

AD _____

Award Number: DAMD17-97-1-7304

TITLE: Simulation, Measurements and Image Processing for
Capillary Optical Digital Mammography

PRINCIPAL INVESTIGATOR: A Suprami, Ph.D.

CONTRACTING ORGANIZATION: State University of New York
Albany, New York 12222

REPORT DATE: July 2000

TYPE OF REPORT: Final

PREPARED FOR: U.S. Army Medical Research and Materiel Command
Fort Detrick, Maryland 21702-5012

DISTRIBUTION STATEMENT: Approved for Public Release;
Distribution Unlimited

The views, opinions and/or findings contained in this report are
those of the author(s) and should not be construed as an official
Department of the Army position, policy or decision unless so
designated by other documentation.

20010620 134



Record Retrieved

Document Title : Simulation, Measurements and Image Processing for Capillary Optical Digital Mammography

[**<- Previous Hit**](#)

(This is hit 5 of 5.)

AD Number: ADA391352

Subject Categories: MEDICINE AND MEDICAL RESEARCH MEDICAL FACILITIES, EQUIPMENT AND SUPPLIES COMPUTER PROGRAMMING AND SOFTWARE OPTICS

Corporate Author: STATE UNIV OF NEW YORK AT ALBANY

Title: Simulation, Measurements and Image Processing for Capillary Optical Digital Mammography

Descriptive Note: Final rept. 1 Sep 1997-31 Dec 2000 Annual (1 Sep 99 - 31 Aug 00)

Personal Authors: Suprami, A.

Report Date: JUL 2000

Pages: 72 PAGES

Contract Number: DAMD17-97-1-7304

Monitor Acronym: XA

Monitor Series: USAMRMC

Descriptors: *COMPUTERIZED SIMULATION, *OPTICAL PROPERTIES, *CAPILLARITY, *MEDICAL COMPUTER APPLICATIONS, *MAMMOGRAPHY, FREQUENCY, IMAGE PROCESSING, SIMULATION, DIGITAL SYSTEMS, SPATIAL DISTRIBUTION, OPTICS, SCATTERING, FIBERS, CONTRAST, REMOVAL, OPTIMIZATION, HIGH RATE, MANUFACTURING, EFFICIENCY, PROTOTYPES, GLASS, DEFECTS(MATERIALS), PROFILES, MONOLITHIC STRUCTURES(ELECTRONICS), ARTIFACTS, BORON OXIDES, SILICATES, MAGNIFICATION, HIGH ANGLES, LEAD(METAL).

Abstract: An extensive computer modeling for polycapillary optics that includes realistic models for the effects of profile defects shows good agreement with measured data. Measured polycapillary fiber transmission is in excess of 65% at 20 keV for borosilicate glass optics, and is in excess of 42% for short leaded glass optics. Measured high angle transmission which corresponds to scatter transmission is lower than 1% for 12 cm long borosilicate optics at 20 keV and less than 4% for 3 cm long leaded glass optics at 80 keV. A long prototype borosilicate magnifying tapered monolithic optic has demonstrated contrast enhancement due to removal of scatter transmission, while at the same time increasing the system MTF performance at all spatial frequencies. Computer modeling, measurement and defect studies have led to better manufacturing capabilities for monolithic optics. The newly magnifying monolithic optics have a high transmission efficiency. Multitaper optics have been produced and tested. Image analysis have provided the means for the image artifact analysis and reduction.

Limitation Code: APPROVED FOR PUBLIC RELEASE

Source Code: 256850

Citation Creation Date: 05 JUL 2001

Hard Copy Cost

REPORT DOCUMENTATION PAGE

Form Approved
OMB No. 074-0188

Public reporting burden for this collection of information is estimated to average 1 hour per response, including the time for reviewing instructions, searching existing data sources, gathering and maintaining the data needed, and completing and reviewing this collection of information. Send comments regarding this burden estimate or any other aspect of this collection of information, including suggestions for reducing this burden to Washington Headquarters Services, Directorate for Information Operations and Reports, 1215 Jefferson Davis Highway, Suite 1204, Arlington, VA 22202-4302, and to the Office of Management and Budget, Paperwork Reduction Project (0704-0188), Washington, DC 20503

1. AGENCY USE ONLY (Leave blank)			2. REPORT DATE : July 2000	3. REPORT TYPE AND DATES COVERED Final (1 Sep 97 - 31 Dec 00)
4. TITLE AND SUBTITLE Simulation, Measurements and Image Processing for Capillary Optical Digital Mammography			5. FUNDING NUMBERS DAMD17-97-1-7304	
6. AUTHOR(S) A Suprami, Ph.D.				
7. PERFORMING ORGANIZATION NAME(S) AND ADDRESS(ES) State University of New York Albany, New York 12222			8. PERFORMING ORGANIZATION REPORT NUMBER	
E-MAIL: cx1122@cnsvax.albany.edu				
9. SPONSORING / MONITORING AGENCY NAME(S) AND ADDRESS(ES) U.S. Army Medical Research and Materiel Command Fort Detrick, Maryland 21702-5012			10. SPONSORING / MONITORING AGENCY REPORT NUMBER	
11. SUPPLEMENTARY NOTES				
12a. DISTRIBUTION / AVAILABILITY STATEMENT Approved for public release; distribution unlimited				12b. DISTRIBUTION CODE
13. ABSTRACT (Maximum 200 Words) An extensive computer modeling for polycapillary optics that includes realistic models for the effects of profile defects shows good agreement with measured data. Measured polycapillary fiber transmission is in excess of 65% at 20 keV for borosilicate glass optics, and is in excess of 42% for short leaded glass optics. Measured high angle transmission which corresponds to scatter transmission is lower than 1% for 12 cm long borosilicate optics at 20 keV and less than 4% for 3 cm long leaded glass optics at 80 keV. A long prototype borosilicate magnifying tapered monolithic optic has demonstrated contrast enhancement due to removal of scatter transmission, while at the same time increasing the system MTF performance at all spatial frequencies. Computer modeling, measurement and defect studies have led to better manufacturing capabilities for monolithic optics. The newly magnifying monolithic optics have a high transmission efficiency. Multitaper optics have been produced and tested. Image analysis have provided the means for the image artifact analysis and reduction.				
14. SUBJECT TERMS Breast Cancer				15. NUMBER OF PAGES 72
				16. PRICE CODE
17. SECURITY CLASSIFICATION OF REPORT Unclassified	18. SECURITY CLASSIFICATION OF THIS PAGE Unclassified	19. SECURITY CLASSIFICATION OF ABSTRACT Unclassified	20. LIMITATION OF ABSTRACT Unlimited	

3. Table of Contents

1. Front Cover.....	1
2. Report Document Page.....	2
3. Table of Contents.....	3
4. Introduction.....	4
5. Body.....	5
5.1. Defect Simulation.....	5
5.2. Simulation of Multifiber Optics.....	14
5.3. Magnifying Linear Monolithic Antiscatter Optics.....	15
5.3.1. Transmission.....	15
5.3.2. Scatter Fraction and Contrast Enhancement Measurements.....	19
5.3.3. MTF Calculation	21
5.3.4. Simulation.....	23
5.3.5. Potential for Lead Glass.....	25
5.3.5.1.Calculation of contrast Improvement and relative SNR.....	26
5.3.5.2. Performance of Three Hypothetical Lenses.....	28
5.3.5.3. Leaded Glass Single fiber Measurements and Analysis.....	30
6. Key Research Accomplishments.....	34
7. Reportable Outcomes.....	34
7.1. Manuscripts.....	35
7.2. Presentations.....	36
7.3. Poster Presentations.....	36
7.4. Employment/Research Received.....	36
7.4.1. Research Employment.....	36
8. Conclusions.....	36
9. References.....	37
10.Appendices.....	40

4. Introduction

At the present time the best way to fight breast cancer is through early detection. The size of malignancies in the early stage is very small, and the absorption of x rays by the malignancies and the breast tissue is similar. Thus high contrast and good resolution are especially important in mammography. In current digital mammography systems, contrast loss occurs from scattered x rays that strike the detector from all directions, and resolution is limited by the pixel size of the digital detector for computed radiography phosphor plates (CR plates), or the conversion efficiency and total number of pixels for visible light CCD systems.

Capillary x-ray optics use total external reflection to guide x rays through tiny hollow glass tubes, similar to the way conventional fiber optics transmit light. A capillary lens is a bundle of hollow glass tubes with channel sizes as small as few microns. The critical angle for total external reflection is as small as a few mrad (1.5mrad for 20 keV photons).^{1,2} A capillary lens can provide almost total scatter rejection. A well-designed lens can also provide magnification without image degradation from a finite source spot size. Thus the effective resolution can be improved while a CR plate is used. Capillary optics can also demagnify the image to match a direct area detector, such as a CZT detector^{3,4}, which maybe available in the near future. Unlike the fiber-optic-CCD combination, this system does not involve the use of a phosphor to convert the x rays to visual light. The solid state detector can provide almost 100% quantum efficiency.

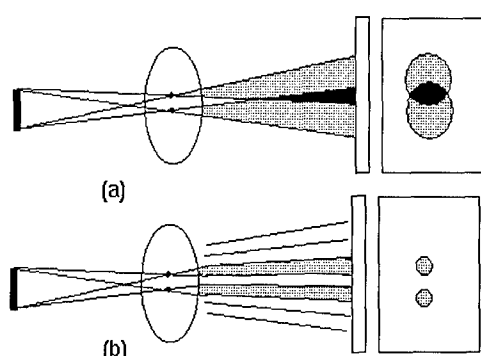


Figure 1 a) Image blurring in normal airgap magnification. b) Capillary lens between the patient and detector eliminates the focus spot blurring.

combining several small pieces. So a better understanding of lens behavior is necessary. Theoretical simulation has been proved to be very helpful in understanding the capillary and lens behavior, and provide feedback to the manufacturing process. It would also be easier to manufacture large lenses if they were shorter; for that reason, lead glass optics, which would stop scattered radiation with a shorter length, were investigated.

The proposed work is focused on lens measurements, computer simulations and image processing. During the first year of the work, a lens simulation has been developed and applied to the experimental data. The simulation has proved to be helpful to understand the lens behavior. MTF is usually measured by taking an image of a slit. It is difficult to measure a stationary lens with this method when the transmission of the lens is not uniform. A method to measure MTF by taking an edge image was developed with background deduction technique. The lens simulation was expanded in the second year, and lead glass optics were investigated. During the second year, the principal investigator was changed from Dr. Lei Wang to Dr. Hui Wang, and the third year the principal investigator was changed from Dr. Hui Huang to Dr. Suparmi.

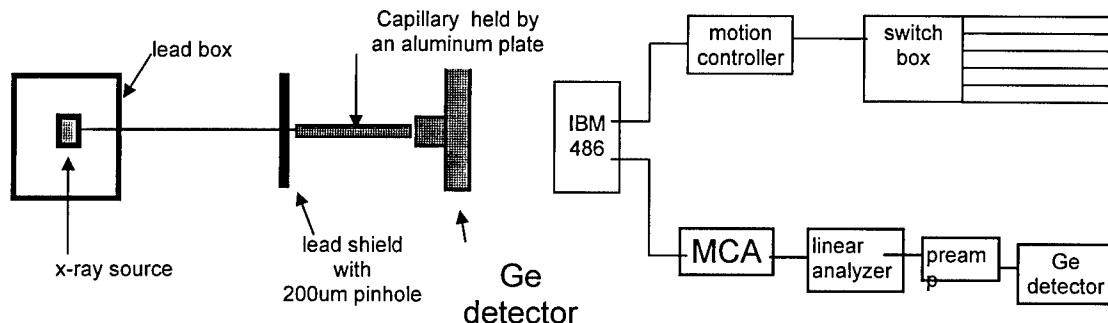


Figure 2. Experimental setup.

Figure 3 Electronic system.

5. Body

5.1. DEFECT SIMULATION

An important step in optics development was the breakthrough in modeling capacity, which has led to an unprecedented level of theoretical understanding of the basic properties of polycapillary fibers, especially fiber defects. To evaluate the experimental performance of polycapillary fibers, and design capillary optics, it is necessary to be able to predict theoretical behavior for complex geometries. The modeling program for single fibers is based on a Monte Carlo simulation of simple geometrical optics. The computational speed is greatly enhanced by a reduction to two dimensions by projecting the trajectory onto the local fiber cross-section.⁷ Reflectivities are computed from standard tables.⁸ Significant recent progress has been made in understanding the effect of capillary profile error, waviness, and roughness on the transmission spectra.⁹ This is extremely important in providing feedback to the manufacturing process. It has been found that extremely good fits can be produced with only two fitting parameters if a more physical model of waviness is employed.¹⁰

The experimental arrangement for single capillary measurements is shown in Figure 2 and Figure 3. An optical rail affixed to an optical table carries an x-ray source, fiber platform, and x-ray detector. Each can be positioned independently in three dimensions. A collimator is placed before the fiber and any remaining x-ray leakage

Type	Description	Outer Diameter, mm	Channel Size, μm	Open Area	Length, mm
A	Borosilicate	0.5	12	65%	105
B	Lead glass	0.5	12	52%	95
C	Borosilicate	0.75	22	50%	136
D	Borosilicate	4	12	55%	130
E	Borosilicate	0.3	4-5	55%	105

Table 1. Description of polycapillary fibers.

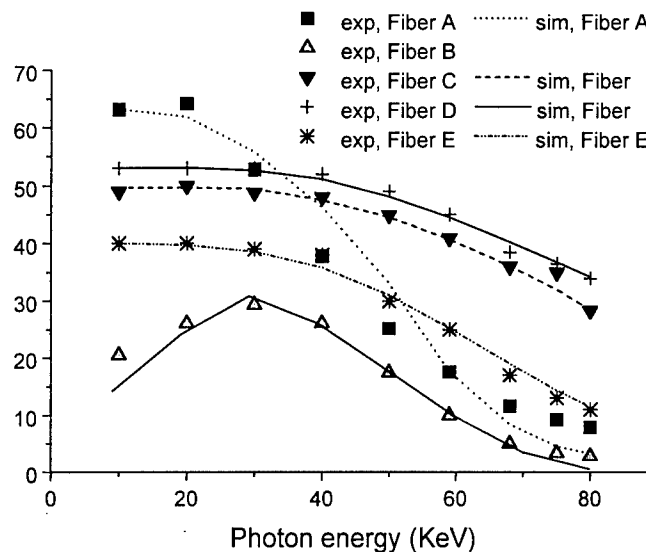


Figure 4. Measured transmission versus energy for polycapillary fibers listed in Table 1.

energies. Modeling this transmission spectra has lead to a greater understanding of defects in polycapillary optics.

In Figure 5, simulations with or without roughness corrections are compared with the experimental data. In these measurements the source is scanned transverse to the fiber axis. The simulation with a roughness height of 0.5 nm fits the experimental data quite well. It is definitely over-corrected when the roughness is 1.0 nm. The same simulations, shown in Figure 7, are also carried out at 68 keV, where the width of the curve is narrower than that at 10 keV because of the smaller critical angle. As a result, photons also experience fewer bounces on average. Simulations with roughnesses as

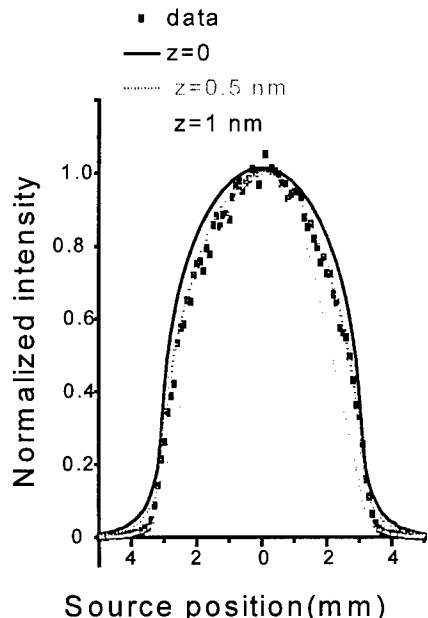


Figure 5. Source scans at 10 keV.

around the fiber is eliminated with metal powder or filings. The measured fibers are described in Table 1.

The results of transmission studies as a function of photon energy are shown in Figure 4.^{11,12} All of the fibers except the lead glass have transmissions at 20 keV nearly equal to their fractional open area (the fraction of the cross section of the capillary which is open space, the rest being glass walls). This transmission corresponds to the primary transmission expected for a linear capillary optic employed as an antiscatter grid.

The transmission falls off at higher

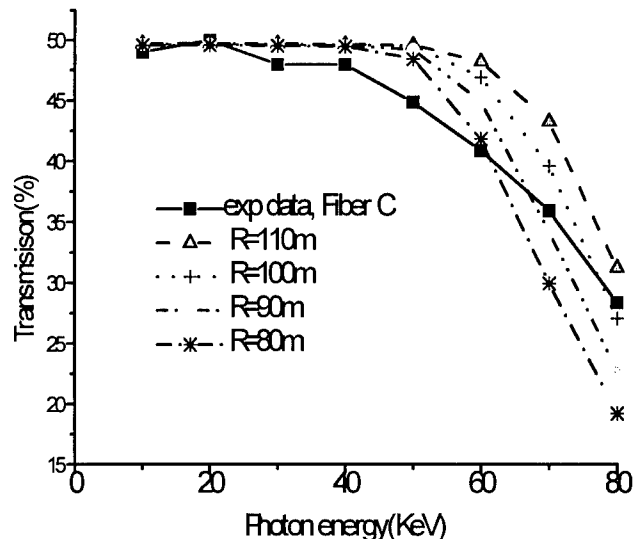


Figure 6. Transmission spectra of Fiber 3 simulated with different bending curvature alone and compared with experimental data

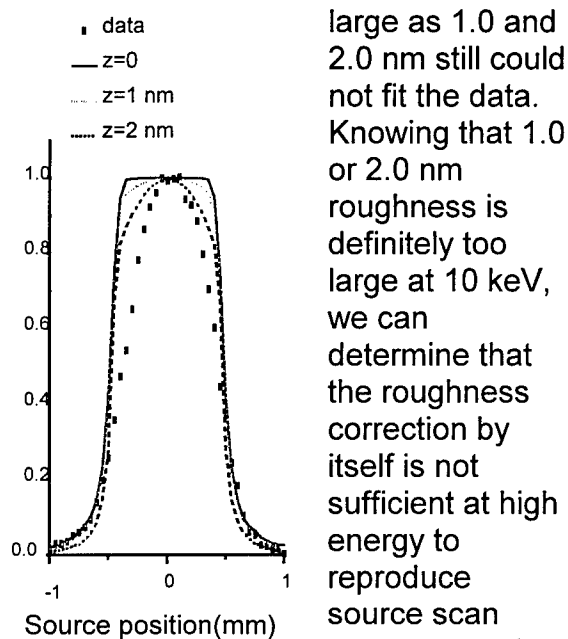


Figure 7. Source scans at 68 keV.

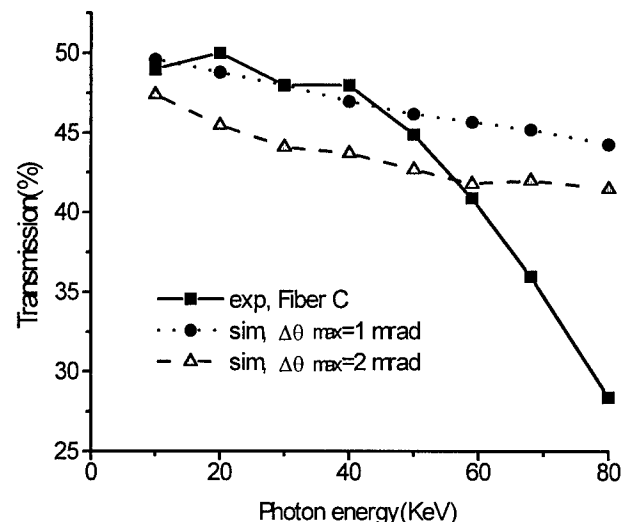


Figure 8. Simulations of transmission spectra with waviness only compared with the experimental data.

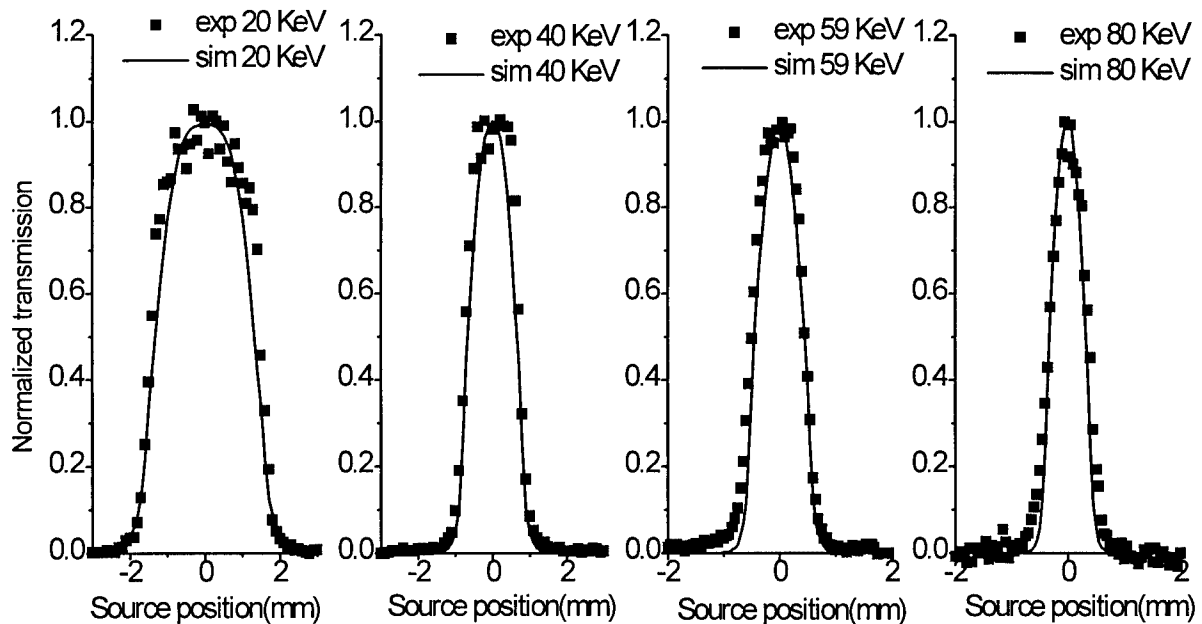


Figure 9. Simulated source scan curves compared with experimental data at four different photon energies. Parameters are: $R = 125$ m, $\Delta\theta_{\max} = 0.35$ mrad, roughness height = 0.5 nm.

A slight bending of the capillary can dramatically reduce the transmission of high energy photons because of the small critical angle. A comparison between experimental data and simulations with different bending is shown in Figure 6. The figure shows that the simulations with bending alone do not fit the experimental data well, which indicates that bending is not the only factor which causes the high energy transmission to drop. However, from Figure 6, we can see that the range of the bending radius must be larger than 100m to give the observed transmission at the highest energy(80KeV).

Capillary surface oscillations with wavelengths shorter than the capillary length and longer than the wavelength of the roughness are called waviness. The detailed shape of waviness is unknown. Its average effect can be considered as a random tilt of the glass wall, so that the grazing angle of the photon is changed by a random amount, $\delta\theta$, after every bounce. $\delta\theta$ is a random number between $-\Delta\theta_{\max}$ and $\Delta\theta_{\max}$ if $\theta \geq \Delta\theta_{\max}$. The maximum random tilt angle $\Delta\theta_{\max}$ is an adjustable parameter which depends on the waviness of the polycapillary fiber. To keep θ' positive, $\delta\theta$ is taken to be a random number between $-\theta$ and $\Delta\theta_{\max}$ when $\theta < \Delta\theta_{\max}$. Since a photon with a incident angle smaller than $\Delta\theta_{\max}$ has a larger chance to experience an angle increase than an angle decrease, this is physically reasonable. In Figure 8, simulations with waviness

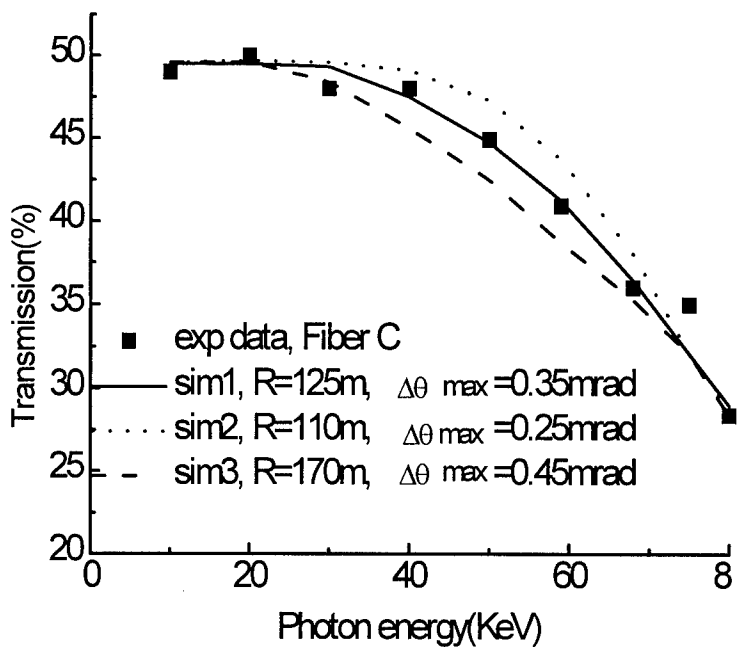


Figure 10. Simulated transmission spectra with different bending and waviness compared with the experimental data in search for the best fitting of Fiber C.

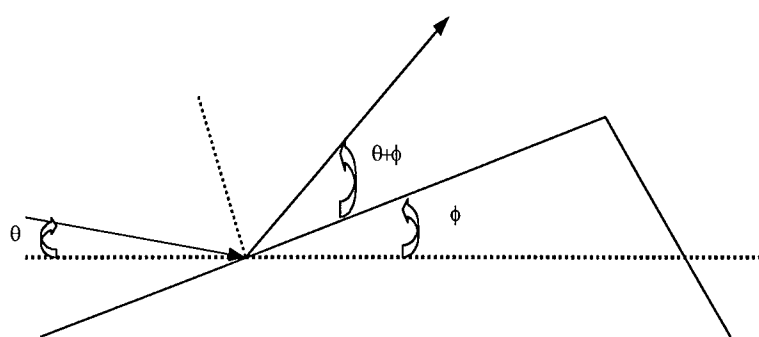


Figure 11. Scheme of an x-ray beam interacts with a random tilt surface.

corrections with $\Delta\theta_{\max}$ set at 1 mrad and 2 mrad, which is comparable to the critical angle, are compared with the experimental data. This figure shows that simulations with waviness alone do not fit the experimental data. This is because the waviness correction changes the reflected angle, not the profile. In fact the capillary is still considered to be straight, so those photons which have few

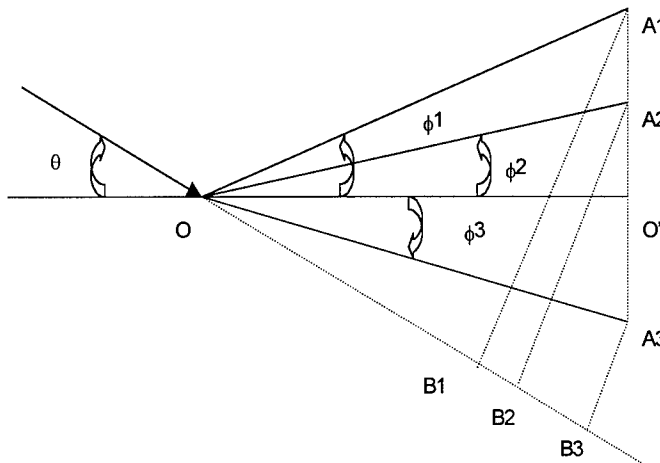


Figure 12. Three surfaces, OA_1 , OA_2 and OA_3 , with different tilt angles, ϕ_1 , ϕ_2 and ϕ_3 , respectively, from the nominal surface OO' .

more photon energies. They all fit quite well. This model, hereafter labeled M1, assumed a uniform distribution of tilt angles, which is not quite physical. In more recent work, discussed as Model M2, it is assumed that these tilt angles, ϕ , are normally distributed in the range $(-\pi/2, \pi/2)$ with the mean value equal to zero. For high quality optics, the standard deviation of this normal distribution, σ , is much smaller than the critical angle, θ_c . The probability distribution of tilt angles, ϕ , is

$$G(\phi) = \frac{1}{\sigma \sqrt{2\pi}} e^{-\frac{\phi^2}{2\sigma^2}}. \quad (1)$$

In this work, Model M2, consideration was taken of the fact that the surface tilt angle will affect the probability of x-ray impact on that surface. Taken to extremes, a surface region perpendicular to the beam is much more likely to intercept the beam than a surface region parallel to the beam. Figure 12 displays three surfaces, OA_1 , OA_2 and OA_3 , with different tilt angles, ϕ_1 , ϕ_2 and ϕ_3 , respectively, from the nominal surface OO' . The projections onto the nominal surface for the three surfaces are equal, $OA_1 \cdot \cos\phi_1 = OA_2 \cdot \cos\phi_2 = OA_3 \cdot \cos\phi_3 = OO'$. The probability of incidence of a parallel x-ray beam with incident angle θ (with respect to the nominal surface OO') hitting these tilted surfaces is given by their corresponding perpendicular length $A_j B_j$ (for $j = 1, 2$ or 3)

$$P_j \propto A_j B_j = OA_j \cdot \sin(\theta + \phi_j) = \frac{OO}{\cos\phi_j} \cdot \sin(\theta + \phi_j), \quad (2)$$

We call this the tilt-corrected probability distribution. The complete description of this distribution is

$$H(\phi) = \begin{cases} \frac{F \sin(\theta + \phi)}{\cos(\phi)}, & -\theta < \phi < \frac{\pi}{2} \\ 0, & -\frac{\pi}{2} < \phi \leq -\theta \end{cases}, \quad (3)$$

reflections will not be significantly effected by waviness.

Finally the waviness and bending are combined by increasing the bending radius R , roughly determined in Figure 6, and adding a waviness parameter, $\Delta\theta_{\max}$. Several trials are shown in Figure 10. Sim2 has too much bending and not enough waviness; sim3 has too much waviness and not enough bending; sim1 is the best fit. Roughness is also included in those simulations. The source scan simulation with the three fixed parameters are plotted along with the experimental data in Figure 9 for four

where θ is the incident angle, ϕ is the tilt angle and F is a normalization constant.

Combining the normal distribution $G(\phi)$ with the tilt correction $H(\phi)$ gives ϕ for a certain incident angle θ as follows:

$$J(\phi) = \begin{cases} Ke^{\frac{-\phi^2}{2\sigma^2}} \cdot \frac{\sin(\theta + \phi)}{\cos\phi}, & -\theta < \phi < \frac{\pi}{2}, \\ 0, & \frac{\pi}{2} \leq \phi \leq -\theta \end{cases} \quad (4)$$

where θ is the incident angle, ϕ is the tilt angle and K is a normalization constant.

Noting that

$$\frac{\sin(\theta + \phi)}{\cos\phi} = \sin\theta + \cos\theta \cdot \tan\phi \quad (5)$$

and that both the incident angle, θ , and the tilt angle, ϕ , are very much less than 40 mrad, we use the approximation

$$P(\phi) = \begin{cases} Ce^{\frac{-\phi^2}{2\sigma^2}} * (\theta + \phi), & -\theta < \phi < \frac{\pi}{2}, \\ 0, & \frac{\pi}{2} \leq \phi \leq -\theta \end{cases} \quad (6)$$

where the normalization constant, C , is

$$C \approx \frac{1}{\sqrt{2\pi\theta\sigma + 2\sigma^2}}, \quad (7)$$

to speed the calculation. $P(\phi)$ is called the tilt-corrected normal distribution. In model M2, σ is the variable that describes the amount of waviness. An example of $J(\phi)$ and $P(\phi)$ is shown in *Figure 13*. The result of the waviness calculation is shown in *Figure 14*. The model M2 shows a much larger drop at high photon energies for lower values of the waviness than does model M1.

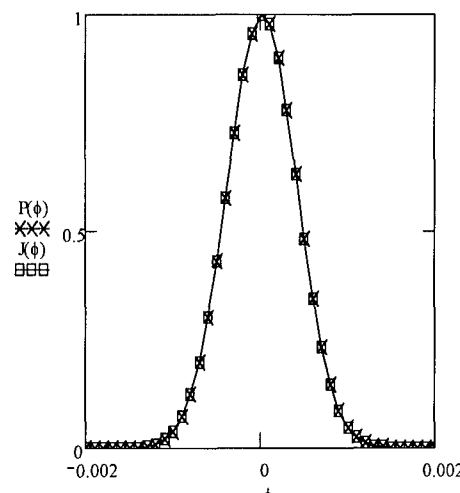


Figure 13. $P(\phi)$ and $J(\phi)$ versus tilt angle ϕ when incident angle $\theta = 0.009\text{rad}$, standard deviation $\sigma = 0.0004\text{rad}$. ϕ is in rad.

A comparison of the simulation with bending and waviness to the experimental data is shown in Figure 15.

Using a similar technique, the simulation was compared to the fibers listed in Table 1, using the parameters listed in Table 2. The results are plotted in Figure 16 and Figure 17. In Figure 16, the transmission for fiber A shows a rapid drop for energies above 30 keV. Although fiber D has lower fractional open area than fiber A, its transmission exceeds that of fiber A at energies above 30 keV. This is because fiber A is thin (0.5 mm in outer diameter) and flexible, therefore difficult to keep straight in the measurement apparatus. Model M2, which can vary only bending and waviness, requires a much sharper bend for fiber A than for fiber D. This bending is more significant at high energies, where the critical angles are smaller.

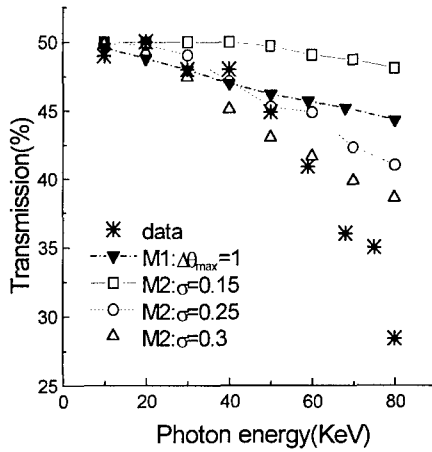


Figure 14. Simulations of transmission spectra for fiber C with only waviness compared with the experimental data. This figure shows the effects of waviness. It also shows simulations using waviness alone do not fit the data. The simulations do not include roughness or bending.

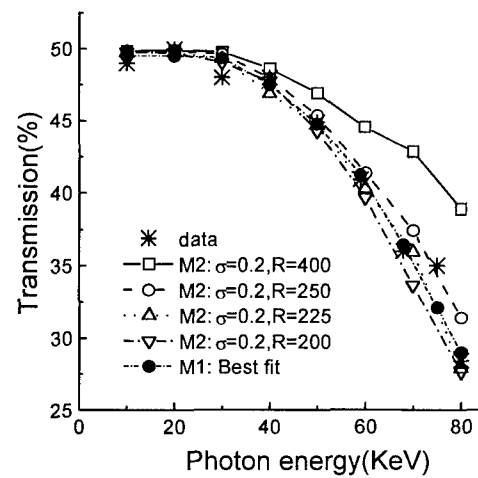


Figure 15. Simulated transmission spectra using model M2 with fixed waviness ($\sigma = 0.2$ mrad) and different bending (bisection method), compared with the experimental data. The simulation curves shown are just a few representative cases in the bisection process. For M2, the best-fit parameters are $\sigma = 0.2$ mrad and $R = 225$ m; for M1, they are $z = 0.5$ nm, $s = 6$ μm , $\Delta\theta_{\text{max}} = 0.35$ mrad and $R = 125$ m.

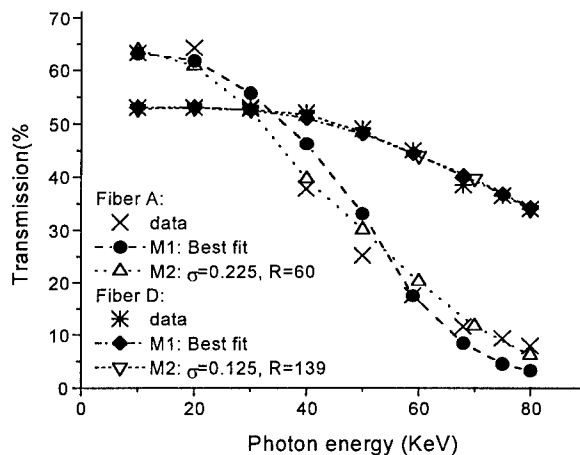


Figure 16. Simulations of transmission spectra of fiber A and fiber D with their best-fit parameters compared with the experimental data. All parameters related to this figure are listed in Table 1.

comparison of fiber C and fiber D. However, if the channel size is too small, as in fiber E, it also results in more reflections being needed for a photon to traverse the fiber and may have introduced other defects such as blocked channels. This is why the transmission is only 40% for the energies below 40 keV although the open area is around 55%.

The new model yields as high a quality fit with two fewer fitting parameters than used in model M1 in Figure 4. The high transmission and the simulation results show that the quality of the capillary fibers is quite good. The bending radius is above 130 meters for type 3 and type 4 capillaries. It is hopeful that we can further improve the high-energy transmission performance of polycapillary fibers by decreasing to an optimum channel size, and making them more rigid.

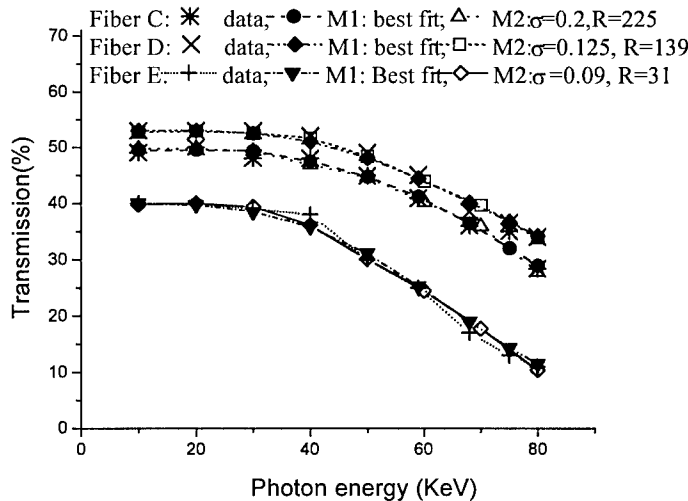


Figure 17. Simulations of transmission spectra of fiber C, fiber D and fiber E with their best-fit parameters compared with the experimental data. All parameters related to this figure are listed in Table 2.

Transmission curves for fiber C and D are similar in shape and are nearly flat up to 60 keV, as shown in Figure 17. However, the smaller channel size for fiber D results in the simulation being less sensitive to bending. Therefore a larger bending curvature (smaller radius) is required for fiber D. The waviness correction for fiber D must therefore be smaller to keep the transmission about the same as for fiber C.

Fiber E is the thinnest fiber. Table 2 shows that it has the largest bending correction because of its flexibility. Its transmission curve is flat up to 40 keV. This is due to its very small channel size, as discussed in the

model M1 in Figure 4. The high transmission and the simulation results show that the quality of the capillary fibers is quite good. The bending radius is above 130 meters for type 3 and type 4 capillaries. It is hopeful that we can further improve the high-energy transmission performance of polycapillary fibers by decreasing to an optimum channel size, and making them more rigid.

Fiber Description						Model M1				Model M2	
Fiber #	Type	Outer Diameter (mm)	Channel Size (μm)	Area	Length (mm)	z nm	s μm	R m	$\Delta\theta_{\max}$ mrad	R m	σ Mrad
A	1	0.5	12	65%	105	0.7	6	105	0.4	60	0.225
C	3	0.75	22	50%	136	0.5	6	125	0.35	225	0.2
D	4	4	12	55%	130	0.8	6	110	0.285	139	0.125
E	5	0.3	4-5	55%	105	0.7	6	28	0.2	31	0.09
F	4	4	12	55%	130	0.8	6	90	0.45	90	0.18

Table 2 Parameters for best-fit simulations. R is the bending radius. For M1, $\Delta\theta_{\max}$ is the amount of waviness, z is the roughness height and s is the roughness correlation length. For M2, σ is the standard deviation of the waviness.

Fiber B in Figure 4 has poor transmission; it is a lead glass fiber, with high surface roughness and waviness. More recently, higher quality lead glass fibers have been produced. The transmission as a function of photon energy for these fibers is shown in Figure 18. These leaded fibers have higher absorption of high angle photons than the lower density borosilicate glass fibers, and therefore would provide even better scatter rejection, as is described in section 0.

Transmission was also measured of deliberately curved fibers, which can be used to deflect x-ray beams over larger angles. The results are shown in Figure 19.

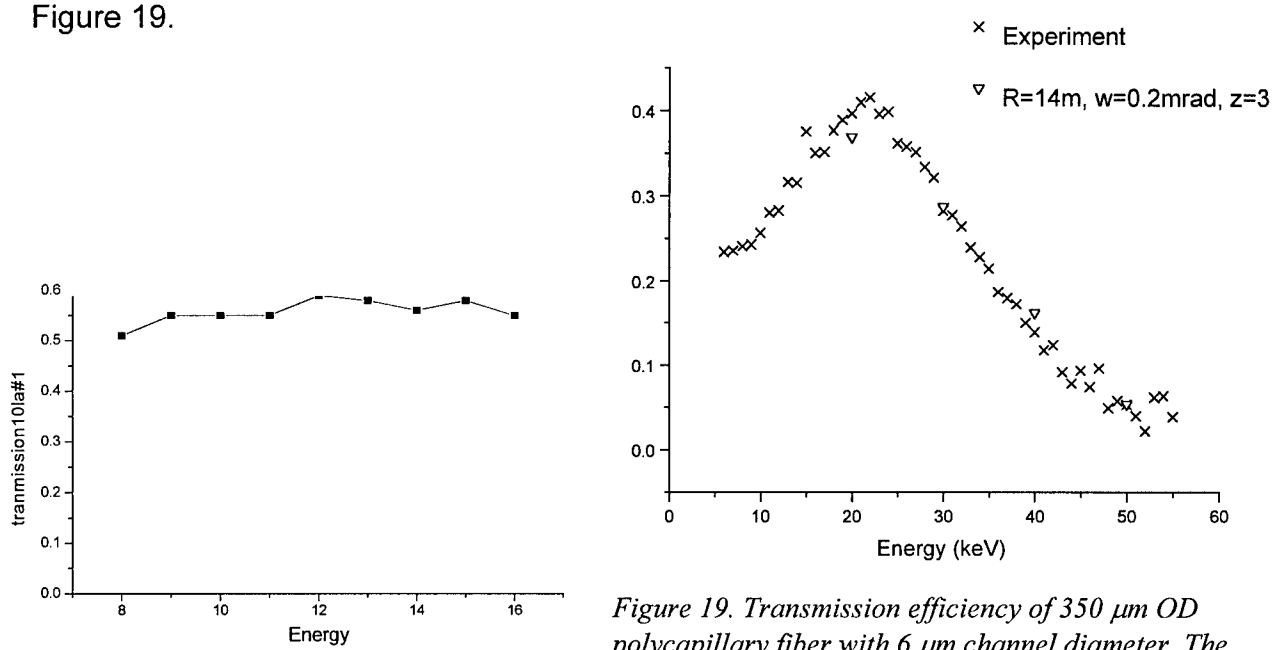


Figure 18. Recently manufactured lead glass fibers.

Figure 19. Transmission efficiency of 350 μm OD polycapillary fiber with 6 μm channel diameter. The fiber length is 25 cm. Simulated values are shown for 20, 30, 40, 50 keV x rays. The parameters are curvature, R ; waviness, w ; and roughness, z .

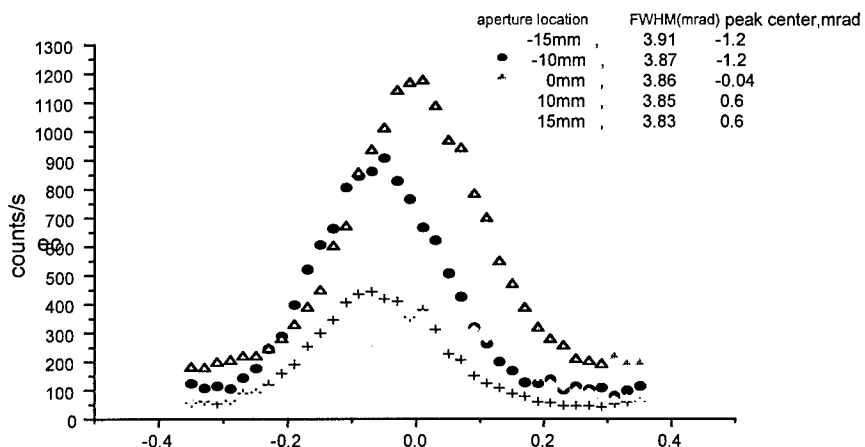


Figure 20. Measured local divergence of the output of multi-fiber I at 8 keV.

Large angular divergence is equivalent to a large focal spot size in a conventional system.

The divergence can also be used to assess fiber alignment in the lens. The beam exiting the optic is characterized by a divergence that arises from two effects. The first is the local divergence of the x-rays emerging from each channel, usually between θ_c , the critical angle for total reflection and $2\theta_c$. There is also fiber misalignment, the deviation of the individual channel axis direction from the optic axis direction. Local divergence depends upon the surface roughness,¹³ waviness, and bending of fibers through the optic. Figure 20 shows the measured local divergence of the output of the collimating lens at 8 keV with the aperture at -15 cm, -10 cm, 0 cm, 10 cm and 15 cm off the axis of the lens. The FWHM of each divergence curve is in the range of 3.8 mrad to 3.9 mrad, which is very close to the critical angle of about 4 mrad at 8 keV. The peak centers of these five local divergence curves are systematically shifted. This shift could be caused by the output ends of the fibers inside the lens being slightly convergent rather than parallel. The widths of the measured local divergence curves shown in

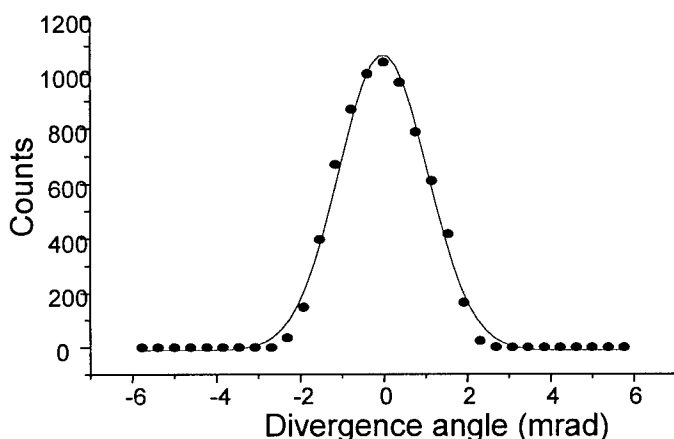


Figure 21. An ideal whole lens simulation at 8 keV gives a divergence FWHM of 2.5 mrad.

5.2. SIMULATION OF MULTIFIBER OPTICS

Measurements of the exit divergence of the collimating optic have been performed at 8 keV and at 20 keV. Exit divergence is important if a capillary optic is to be used as a collector fore slit before the patient. In this case, the spatial resolution will depend on the angular spread of x-rays at the exit end of the polycapillary fibers.

Figure 20 are larger than that predicted by an ideal lens divergence simulation, shown in Figure 21.

The divergence of the modeled ideal lens is low because the nearly straight central fibers, if ideal, would not increase the divergence above the entrance divergence due to the source spot size. Figure 23 shows the simulated divergence profile of x-rays exiting from an ideal straight fiber, which has a FWHM of 2.36 mrad.

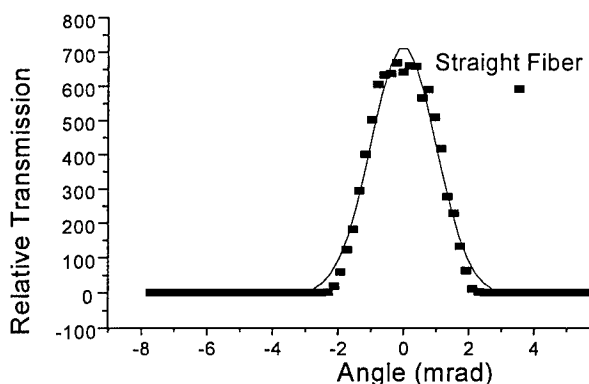


Figure 23. For an ideal fiber (with no surface defects), the divergence simulation yields a FWHM of 2.36 mrad at 8 keV.

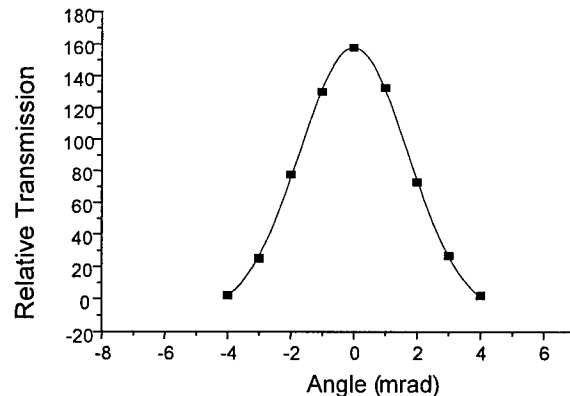


Figure 22. A simulation with a waviness of 0.15 mrad increases the divergence value from 2.4 mrad for an ideal straight fiber to 4.0 mrad.

The simulations in Figure 21 and Figure 23 did not include the effects of profile defects and waviness. Waviness will increase the angle of reflection for x-ray photons for most bounces inside the channel. Consequently the divergence from the lens increases. Figure 22 shows a simulated transmission of a straight fiber as a function of exiting angle, using a waviness of $\omega = 0.15$ mrad. The width of the simulated divergence curve for this straight fiber is about 4.0 mrad, which is close to the local divergence at the center of the lens shown in figure 16. Waviness of the channels changes the divergence of the x rays exiting from the center of the lens from about 2.4 mrad to 4.0 mrad.

5.3. MAGNIFYING LINEAR MONOLITHIC ANTISCATTER OPTICS

5.3.1. TRANSMISSION

Linear monolithic optics taper as a single glass

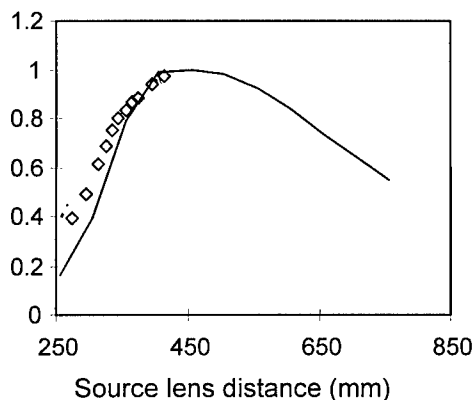


Figure 25. Transmission of tapered lens. Solid line is simulation.

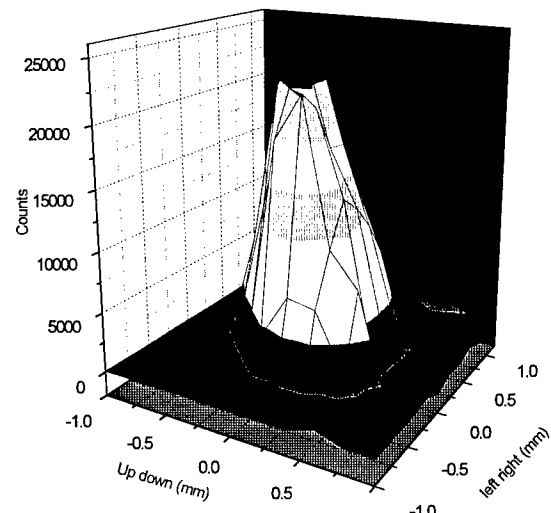


Figure 24. 2-D source scan of early prototype optic (input diameter = 2 mm, output diameter = 3 mm, transmission = 5 % at 20 keV, focal distance 22 cm) This lens transmits poorly because only the central capillary channels transmit while the outer capillaries do not transmit at all. Only about 33 % of the optic cross section transmits at 5 % or greater.

unit from input to output as shown in Figure 28. These optics are relatively difficult to manufacture. Many early prototypes have poor transmission, as shown in Figure 24. To help understand the defect problem an extensive simulation and measurement study was performed on several of the prototypes.

Transmission of a monolithic taper is plotted versus source lens distance in Figure 25 along with the simulation values. The maximum point for transmission is around 450 mm. The second method can be affected by the source instability.

Transmission was measured in a wide energy range for the whole lens as well as the central part of the lens. The transmission spectrum for the whole lens is plotted in Figure 26. The figure shows that the transmission drops quickly for photons with energy higher than 20 keV, but the transmission under 20 keV is almost flat. The low transmission in the high energy range can be explained by the non-linearity of the lens. The outermost channels are more bent than the central channels, so they have low or zero transmission at the

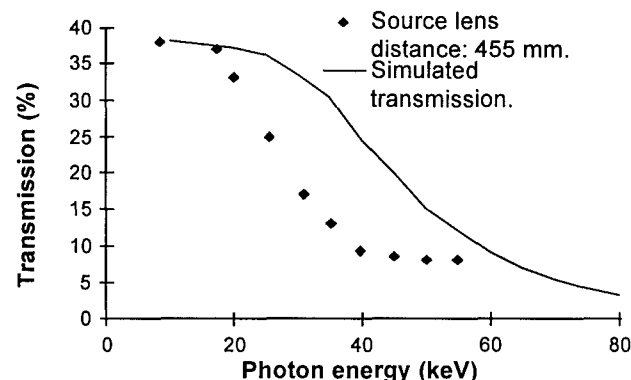


Figure 26. Transmission of whole tapered lens.

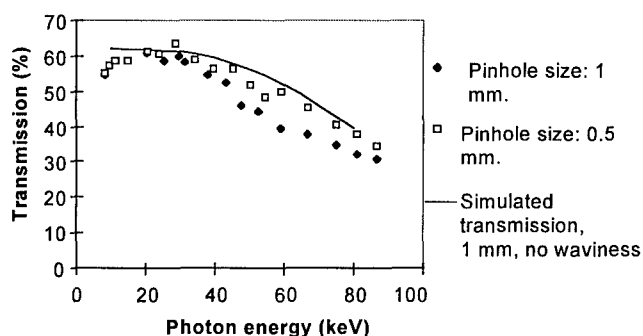


Figure 27. Transmission of the central part of the tapered optic.

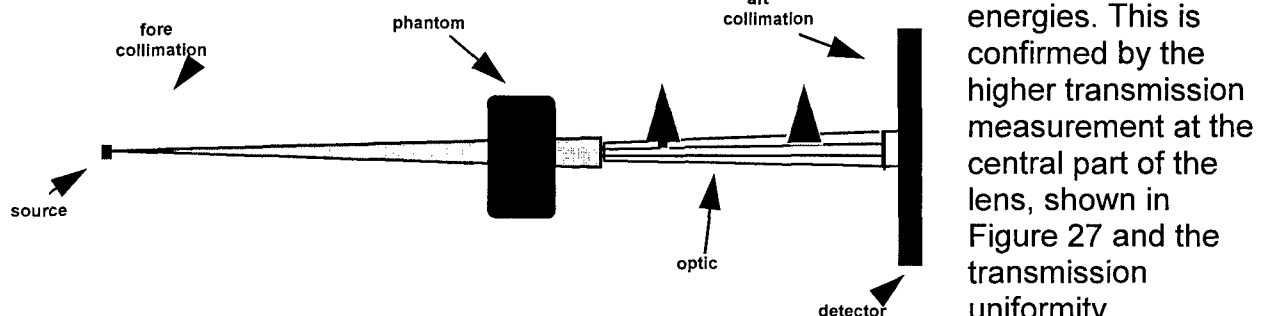


Figure 28. Small optic scanning geometry for contrast and imaging measurements.

uniformity of the lens was measured by putting a 200 μm pinhole in front of the lens and performing a two dimensional scan. At 8 keV, the whole lens transmits, although we can see the transmission is not completely flat due to the non-linearity and the defects of the lens, such as blocked channels. At 25 keV, transmission of the whole lens drops

higher photon energies. This is confirmed by the higher transmission measurement at the central part of the lens, shown in Figure 27 and the transmission uniformity measurement at different energies, shown in Figure 29. Transmission

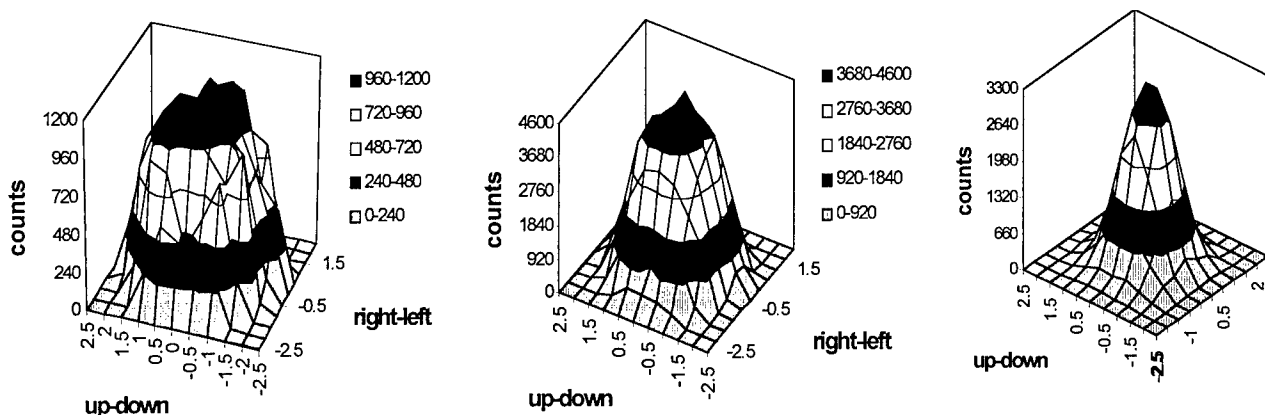


Figure 29. Two dimensional scans of the output of the tapered optic.

to 25%. Most of the lens is still transmitting at 25 keV, but the outer channels have lower transmission than the central part. At 35 keV, the lens has a narrower transmitting region. The measurements show that the lens has undesirable nonlinearity.

5.3.2. Scatter Fraction and Contrast Enhancement Measurements

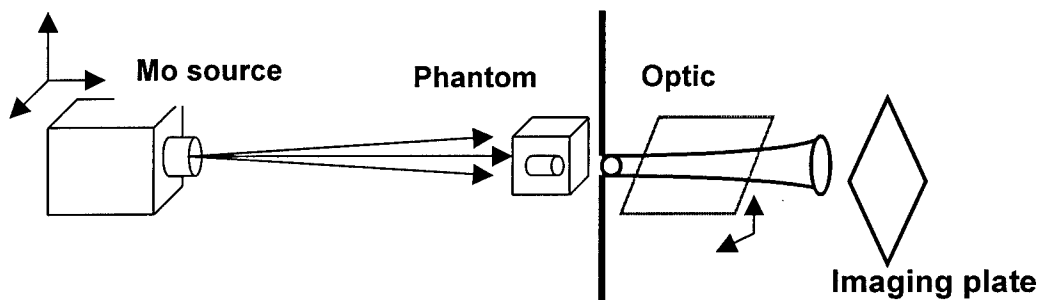


Figure 30. Experimental setup for scatter rejection and contrast measurements

The experimental setup for scatter rejection and contrast measurements is shown in figure 30. The x-ray generator used in the experiment was a Mo source with a 300 μm source spot size and maximum operating voltage of 35 kVp. The source head was mounted on two stages which could be translated in the two directions transverse to the x-ray beam. Thick lead shielding was used to prevent background x rays from reaching the imaging plate. The borosilicate monolithic optic was put on aluminum plate and covered by powder filling to prevent x-ray leakage around the optic. A Fuji imaging plate with 50 μm resolution was used to record the image. The Lucite phantom used in the contrast measurement was 45 mm thick. Several lead strips with different width were attached to the phantom to measure scatter transmission.

A prototype borosilicate monolithic optic, 166 mm in length, with input diameter of 4.5 mm and 7.6 mm output, was used to measure scatter fraction and contrast

enhancement of a Lucite phantom with a thickness of 45 mm. The transmission of the whole optic was 35% at 20 keV and 7% at 60 keV. A central part of the optic, 4 mm in diameter at the output, has good transmission up to energy 40 keV.

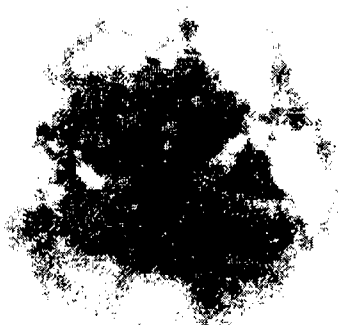


Figure 31. Output uniformity of a long monolithic optic, $L=166$ mm, $D_{input} = 4.5$ mm, $D_{output} = 7.6$ mm

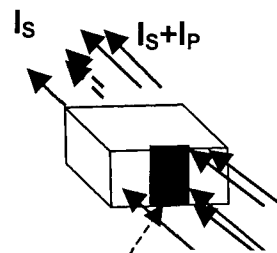


Figure 32. Sketch of X-ray paths for scatter measurement.

optic provides magnification, and thus enhanced resolution, as well as reducing scatter.

The output uniformity of the optic is shown in figure 31. The channels of the outer part of the optic, which does not transmit well, may be blocked by glass inclusions. Such an

5.3.2.1 Scatter Fraction

To measure the scatter transmission of the optic, several lead strips with different width but the same thickness were attached to the phantom, as shown in figure 32. The scatter fraction, S_F , was calculated using formula

$$S_F = I_S / (I_S + I_P) \quad (8)$$

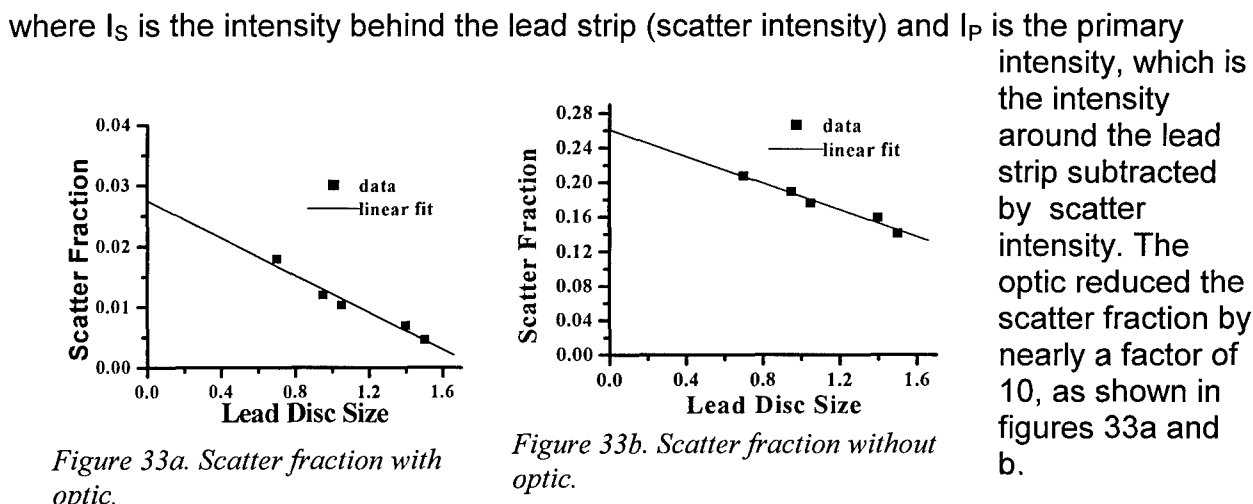


Figure 33a. Scatter fraction with optic.

Figure 33b. Scatter fraction without optic.

5.3.2.2 Contrast

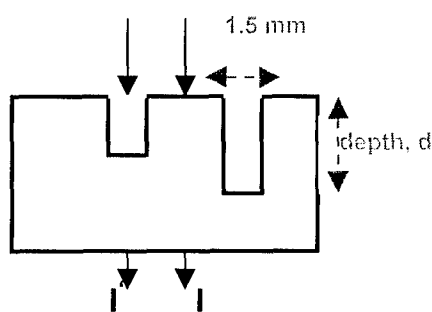


Figure 34. Sketch of Lucite phantom

$d = 20 \text{ mm}$ $d = 35 \text{ mm}$

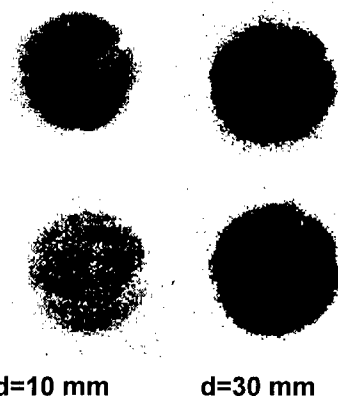


Figure 35a. Lucite phantom image with optic.

was used to magnify the image, reduce the scatter transmission and enhance the contrast.

Hole depth, d (mm)	Contrast		Ratio
	With optic	No optic	
35	3.1 ± 0.1	2.4 ± 0.03	1.3 ± 0.1
30	2.6 ± 0.1	1.9 ± 0.04	1.4 ± 0.1
20	2.1 ± 0.1	1.4 ± 0.1	1.5 ± 0.1
10	1.2 ± 0.03	0.7 ± 0.02	1.7 ± 0.02

Table 3. Contrast and contrast enhancement

The Lucite phantom used in the contrast measurements was 45 mm thick and had four holes with the same diameter of 1.5 mm and different depths, from 10 mm to 35 mm, as listed in Table III. The diameter of the holes were smaller than the central area the optic which transmits well. Each image was taken on a single hole. A sketch of the Lucite phantom with contrast was measured with and without optic. The images with and without the optic are shown in figures 35a and b. The contrast, C , is

$$C = \ln (I' / I) \quad (9)$$



Figure 35b. Lucite phantom image without optic.

where I is the intensity near the hole and I' is the intensity through the hole. The contrast with and without the optic, and also contrast enhancement, are listed in Table 3. The contrast enhancement

is the ratio of the contrast with and without the optic. The results show that the optic increases the contrast by a factor of 1.7 for the shallowest hole. The images in figures 35a and b are shown to scale. A magnification of 1.8 was obtained with the optic. This long monolithic optic with small area

5.3.2.3 Disadvantages of Long Borosilicate Optics

Long optics, even with small input area, tend to have defects as shown in figure 3. A long optic also leads to manufacturing complexity and expense. Improvements in the technology of fabricating monolithic optics have been achieved.¹⁴ Medical imaging or astronomy applications, however, require large area optics. For high-energy applications, borosilicate optics need to be quite long. Leaded glass would allow the optic to be much shorter and still good give scatter rejection because of

strong absorption of lead glass. The shorter optics are easier to manufacture and could be cheaper. In the following section, several leaded glass fibers were measured and analyzed using a geometric simulation.

5.3.3 MTF CALCULATION

Modulation Transfer Function (MTF) is the most fundamental measurement of spatial

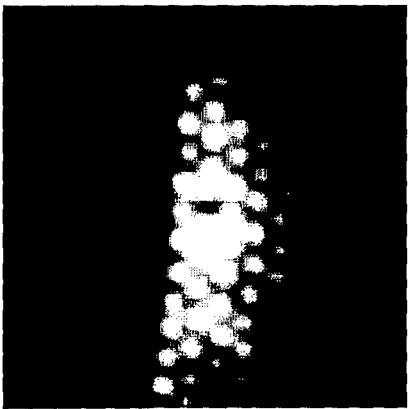
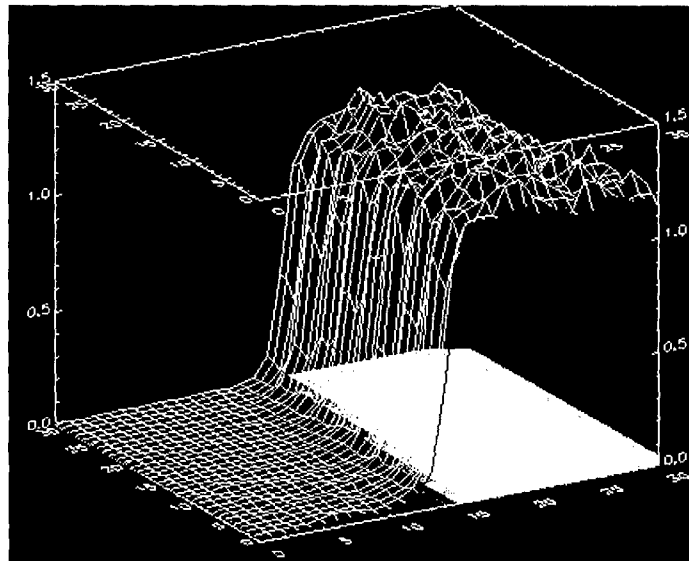


Figure 36. Magnified image of a lead edge. Real image size: 5(mm) X 5(mm).



resolution used in radiology. The standard technique is to image a slit, determine the line spread function (LSF), and compute the Fourier transform. The MTF

measured for the mammography system with capillary optics, compared to that without the capillary optics, will give the resolution improvement and also can be used to diagnose artifacts. The structure of the capillary bundles was obvious. In this case, the LSF could not be obtained by imaging a slit without background elimination. The background deducted slit image is the slit image divided by the image with capillary only. However, this involves image registration. The information for background that can be used for image registration is too little in the slit image. An alternative method is calculating the LSF as the derivation of the edge spread function (ESF). The edge image left enough background for registration so that it could be a feasible method in our case.

Figure 37. Three-dimensional edge image after background subtraction.

The structure of the capillary bundles was obvious. In this case, the LSF could not be obtained by imaging a slit without background elimination. The background deducted slit image is the slit image divided by the image with capillary only. However, this involves image registration. The information for background that can be used for image registration is too little in the slit image. An alternative method is calculating the LSF as the derivation of the edge spread function (ESF). The edge image left enough background for registration so that it could be a feasible method in our case.

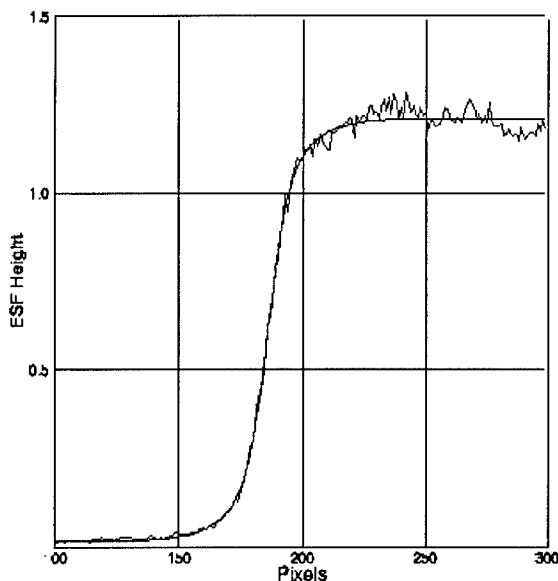


Figure 38. Edge spread function and its fitting curve.

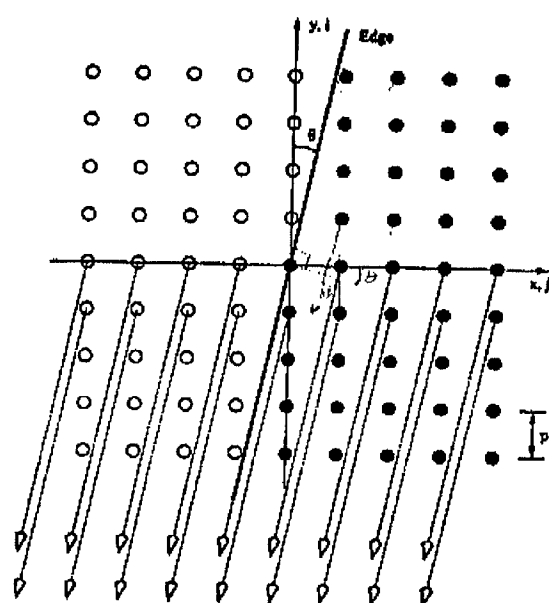


Figure 39. Reprojection of a two-dimensional edge image into a finely sampled ESF.

A registration algorithm (FMI-SPOMF) proposed by Chen, et al.¹⁴ was used in this work. This is a method to match a two-dimensional image to a translated, rotated and scaled image. The approach consists two steps: the calculation of a Fourier-Mellin Invariant (FMI) descriptor for each image to be matched, and then matching of the FMI descriptors. FMI descriptors are translation invariant. The matching of the FMI descriptors is to find out the rotation and scaling, and achieved using a symmetric

phase-only matched filtering (SPOMF). In our case, there is no change in scaling, but rotation is probably involved. When the rotation was found, image translation is found by SPOMF method.

Images were taken with edge as shown in figure 36. The edge was made of a lead plate. The size of each image is fifty by fifty in pixels. They were taken in an experimental digital mammography system with a computed radiography digital phosphor plate. The digital CR plate has limited resolution, 5 lp/mm, and is usually considered to be not good enough for clinical mammography. But the effective resolution of the system could be improved by the magnification of the capillary optics. The magnification of the capillary lens used in the system is 1.86, so that the effective

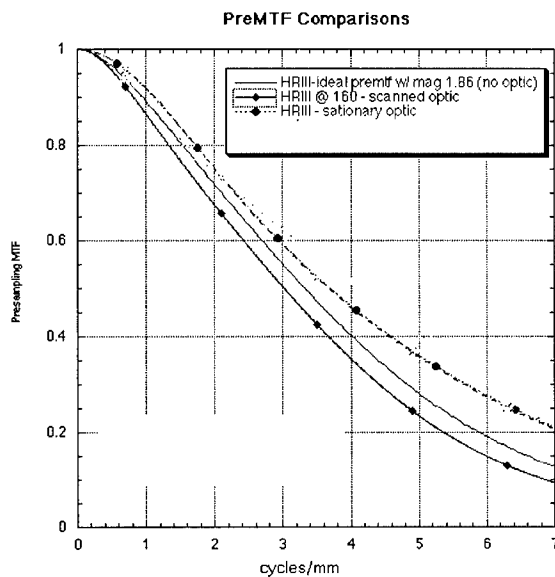


Figure 40. Calculated MTF compared with the MTFs with scan optics, and without optics.

resolution should be improved by a factor of 1.86.

The registration algorithm was implemented in IDL. With the FMI-SPOMF registration algorithm, no rotation was found. The translation was then found by SPOMF algorithm. The difference between the usual correlation method and SPOMF method is that it only uses the phase information. The phase-only correlation function has sharper peak than normal correlation function. Sub-pixel resolution could be achieved theoretically. However it was found that the resolution is not good enough in our case. This may be caused by the relatively small image size. The background-subtracted result was further optimized by manual shifts in sub-pixel range. The result after manual optimization was shown in figure 37. The periodic background is totally gone. A cubic spline interpolation method was used for the best result while shifting the background image relative to the edge image.

The presampling MTF includes unsharpness of the detector and the sampling

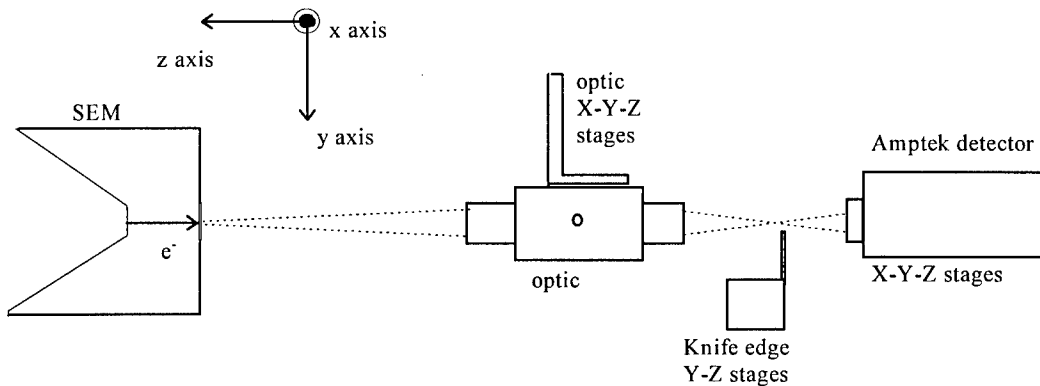


Figure 41. Schematic of the experimental setup for optic characterization.

aperture. In order to eliminate the aliasing, a finely sampled ESF is obtained with a slightly angulated edge in a single exposure as illustrated in figure 39.^{15,16} The angle in our edge image in figure 37 was calculated to be around 6 °. The resultant ESF is plotted in figure 38. A direct calculation of MTF is to take the derivation of the ESF and result a LSF, then take Fourier transform. As it can be seen, the ESF in our case is not smooth enough for a direct calculation. An alternative technique is to use an ESF fitting procedure.¹⁷ In the fitting method, the ESF is represented with a term (1-exp) and an error function (erf) as in equation (10). MFT is calculated by equation (9) where a, b, c and d are fitting parameters from equation (10). The fitting curve is plotted in figure 38 as the solid line.

$$ESF(x) = a\{1 - \exp(-b|x - x_0|)\} + c \cdot \text{erf}(d^{1/2}|x - x_0|) \quad (10)$$

$$MTF(f) = \frac{c \cdot \exp(-\pi^2 f^2 / d) + a(1 + 4\pi^2 f^2 / b^2)^{-1}}{(c + a)} \quad (11)$$

The calculated MTF was compared with that from scanned optics in figure 40. The MTF from scanned optics was calculated from a slit image. Optic structure was smeared out with scanning, so no background deduction is necessary. An ideal MTF was also plotted in figure 40. An ideal MTF is the one when we assume the lens introduces only the 1.86 factor magnification and no image degradation. It is measured with a slit image without optics, and its result was multiplied by the magnification of the capillary lens.

The measured MTF with lens should no better than the ideal MTF. However, for some reason, the MTF for stationary lens is better than the ideal MTF. It is possible that the background elimination process failed the MTF measurement. Another possibility is that the magnification of the lens is different from 1.86, since the magnification was measured separately at a different time.

5.3.4. SIMULATIONS

Modeling defects, including waviness, bending, and blockages, require sophisticated simulations. The simulations plotted in Figure 25 and Figure 26 used the same roughness and waviness correction as that used for fiber D in Figure 4. A linear tapered lens is ideal for mammography, because, as shown above, any curvature can cause transmission reductions. However, the lenses currently available have nonlinear profiles. The profile is not circular, but to simplify the simulation, we assume that the profile is circular. A uniform bending will provide the best transmission performance for a given bending angle, so the simulation will overestimate the lens performance. A further simplification assumes the lens has a fixed channel size, although the channels actually taper with the lens.

The geometry for uniformly bent nonlinear lenses is shown in figure 44. The simulation method for a uniformly bent lens is an extension of the simulation for uniformly bent polycapillary fibers. The simulation is done by sampling channels in the input cross section of the lens with an even step size. In the simulation for a bent fiber it is assumed that the capillary bends in -y direction, and z direction is along the input axis of the fiber. In order to reuse the old simulation code, the coordinate of the simulation x-y-z is rotated to x'-y'-z', where z' is the direction of channel axis at the input end and -y' is the channel bending direction. Assuming the source position and the capillary position at input end is (x_s', y_s', z_s') and $(0, 0, z_i')$ respectively, then the source capillary distance is $z_i' - z_s'$. The origin of the coordinate is selected to be the focus point of the

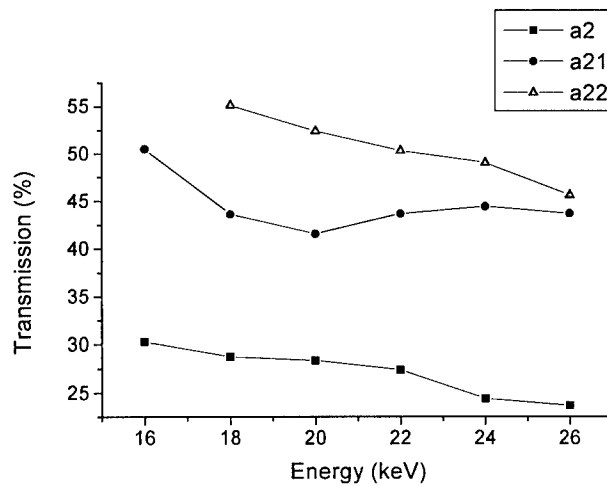


Figure 42. Transmission of final half of A (A2), and its two constituent pieces, the first 5.5 cm, A21 and the final 5.5 cm, A22. A21 contains a defect.

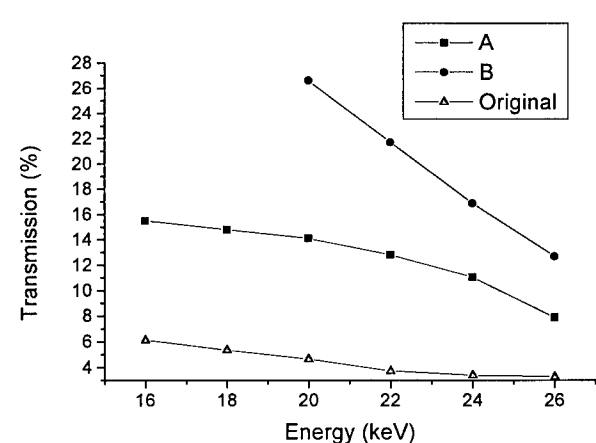


Figure 43. Transmission of original optic compared to two pieces. B is the first 10 cm (closest to the source), A is the final 22 cm.

lens.

Another parameter needed by the simulation is the bending curvature of the selected channel. This value varies with the position of the channel. The calculation of the bending curvature is demonstrated in figure 45.

First it is assumed that the channels are evenly distributed on both input and output cross section. Let input and output diameter of the lens be r_i and r_o , and focal distance $\overline{O'A}$ be f , and the lens length \overline{AC} be L , then

$$\overline{AB} = \sqrt{x_i^2 + y_i^2}, \quad \overline{CE} = \overline{AB} * r_o / r_i$$

$$f / (f + L) = \overline{AB} / \overline{CD}, \quad d = \overline{CE} - \overline{CD}$$

For a small bending angle,

$$\alpha \approx L / R = d / (L / 2)$$

where R is the bending radius, d is the distance between point D and E as shown in Figure, and α is the bending angle. Thus

$$R = L^2 / 2d \quad (12)$$

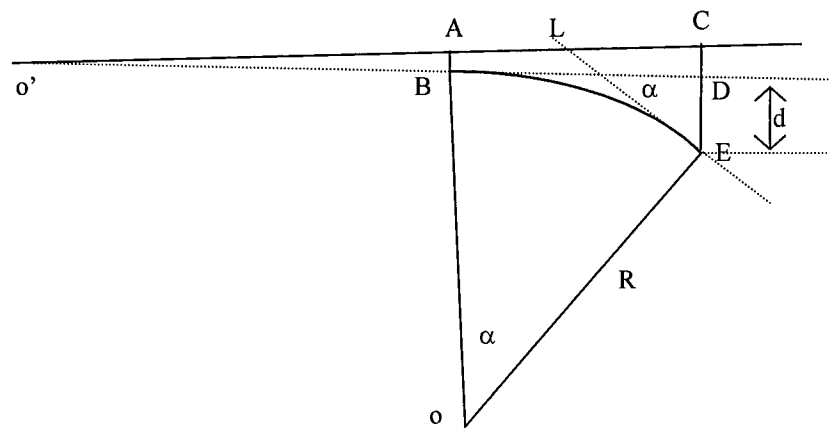


Figure 45. Curvature estimation for lens simulation.

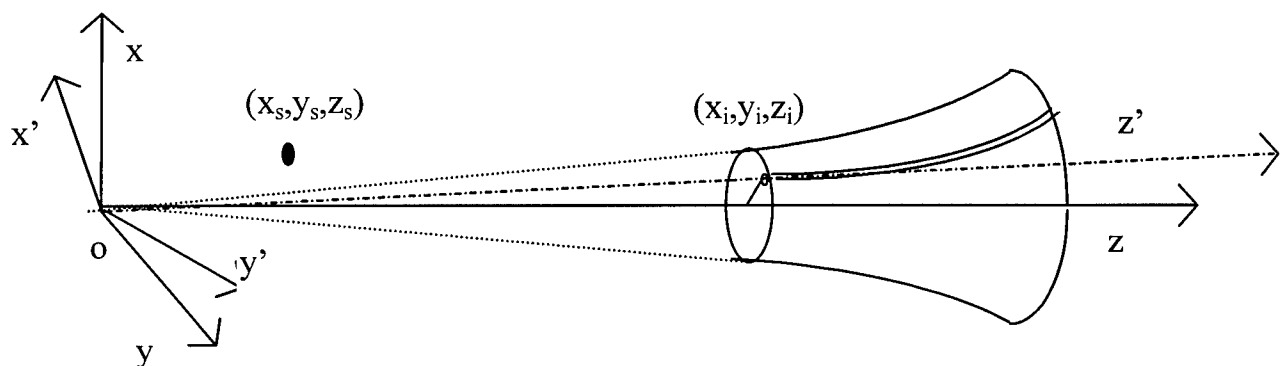


Figure 44. Geometry for lens simulation

The simulated results in Figure 26 and Figure 27 show higher transmission than the experimental results. This indicates that the lens has more reduction in transmission due to the bending. This is expected, because the lens does not have a uniform bending.

5.3.5 POTENTIAL FOR LEAD GLASS

Transmission from early fibers was poor in the whole energy range. Recent fibers are more promising. Transmission for an early 95 mm long and a more recent 125 mm long lead glass polycapillary fiber is shown in Figure. The transmission drop at lower energies may be caused by partially blocked channels. Transmission can also be improved by using a short optic. Almost total scatter rejection is expected for a lead glass optic longer than 30 mm.

5.3.5.1 CALCULATION OF CONTRAST IMPROVEMENT AND RELATIVE SNR

Lenses with large diameters are not currently available. Their potential behavior can be predicted by scaling up existing measurements to a large area lens, as shown in figure 47. The value of h is the length of the optic. For a point P on the film, scattered radiation could come from any direction in the solid angle Ω_{patient} , which is the solid angle subtended by the patient. The transmission for scattered x rays can be calculated from the mass absorption coefficients. The calculated scatter transmission depends on the length of the photon path through the optic. Making a very conservative estimation, we can fix this length to the length of the optic. There is also a small part of the scattered x rays that have almost the same direction as those primary x rays. This part of the scattered x rays with an incident angle less than critical angle could still pass through the channel. So the total scatter transmission of the lens is

$$T_{s-optic} = \frac{N_{s-optic}}{N_s} = T_s + \frac{T_p \cdot \pi \theta_c^2}{\Omega_{\text{patient}}}, \quad (13)$$

where $N_{s-optic}$ is the number of scattered x rays with the optic, N_s is the number of scattered x rays without the optic, T_s is the transmission for large angle scattered x rays, T_p is the transmission for primary x rays, Ω_{patient} is the angle subtended by the patient, θ_c is the critical angle for transmission in the channels. Because the critical angle is on the order of 10^{-3} radians, the second term is very small, and can be ignored. So scatter transmission of the lens can be estimated to be equal to large angle scatter transmission, T_s , which can be calculated from equation 19 and nearly scatter free lenses can be obtained by using a suitable length optic. In the above equation, we assumed that the angular distribution of the scattered x rays is isotropic. If the scatter

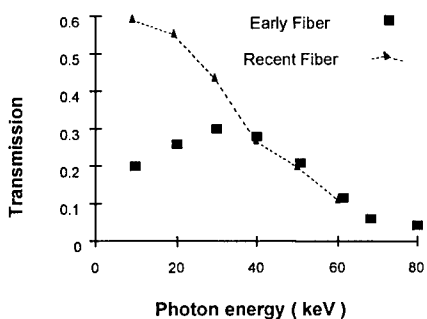


Figure 46. Transmission as a function of photon energy for a lead glass capillary. The fibers are 105-120 mm in length.

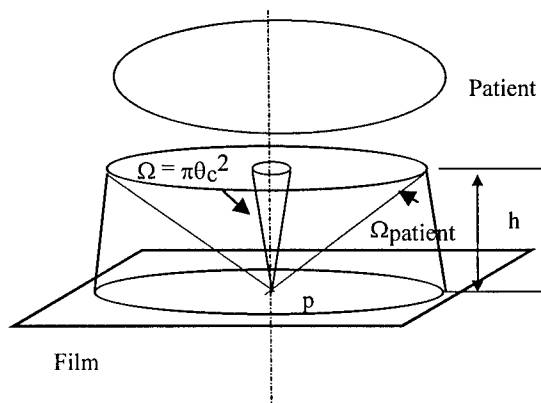


Figure 47. An ideal large area lens.

Table IV. Transmissions for three lenses. The results for the ideal borosilicate lens are measured results for the center part of the prototype lens. The results for lead glass lens are simulated with 120 kVp spectrum and a W target.

Lens #	Lens type	Length (mm)	Photon Energy	Primary transmission $T_{p-optic}$	Scatter transmission $T_{s-optic}$
1	Ideal borosilicate Lens. Scaled up from the center part of the prototype lens	166	20 KeV	0.6	0.0
			45 KeV	0.55	0.002
			60 KeV	0.55	0.005
			70 KeV	0.45	0.03
2	Actual Borosilicate prototype lens	166	20 KeV	0.33	0.0
3	Lead glass	30	69 KeV	0.63	0.0076

distribution is not isotropic, the second term in equation (13) can be larger than expected, but will still be very small, and this assumption will not significantly effect the result. In equation (13) T_s , T_p and θ_c are all energy dependent. In the case where x rays with a wide x-ray spectrum are used, T_s and T_p

should be replaced by the average large angle transmission and primary transmission. To avoid underestimating scatter transmission, θ_c can be set to be the critical angle for the lowest energy in the spectrum.

The scatter and primary transmission of the optic determine the performance of the capillary lens. For example, if the scatter fraction before the capillary lens is F , then the scatter fraction after the lens, F_{optic} , is

$$F_{optic} = \frac{F \cdot T_{s-optic}}{F \cdot T_{s-optic} + (1-F) \cdot T_{p-optic}} = \frac{KF}{1-F(1-K)}, \quad (14)$$

where $T_{p-optic}$ is the primary transmission of the lens and K is the ratio

$$K = \frac{T_{s-optic}}{T_{p-optic}}. \quad (15)$$

The contrast enhancement achieved by using the optics is

$$\frac{C_{optic}}{C_{no-optic}} = \frac{1 - F_{optic}}{1 - F} = \frac{1}{FK + (1-F)}. \quad (16)$$

The contrast enhancement alone is not the only relevant quality factor. The signal to noise ratio (SNR) is another important quality factor. According to the Rose model,

$$k^2 = C^2 \Phi A, \quad (17)$$

where k is the SNR, C is the contrast, Φ is the photon flux, and A is the area of the target. In order to compare the SNR for different scatter rejection devices, relative SNR

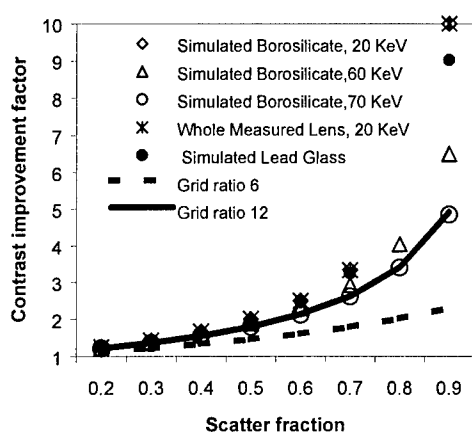


Figure 48. Contrast improvement vs. scatter fraction for the three lenses. The results were compared with the performance of two commercial grids.

5.3.5.2 PERFORMANCE OF THREE HYPOTHETICAL LENSES

Performance estimates of three hypothetical lenses are given in Table IV. The ideal borosilicate lens is scaled up from the center part of the measured lens. Simulated transmission was used for the lead glass lens. The performance of the three lenses was compared with the performance of the conventional grids described in Table V. The primary and scattered transmissions of the different grids in Table V were measured at 69 keV, which is the average energy of the 120 kVp tungsten spectrum, and with scatter fraction of 85%, by C. E. Dick and J. W. Motz.¹⁸ It is assumed that the scatter and primary transmission are the same under different scatter fraction. This assumption is correct if the angular distribution of the scattered x rays does not change. The performance of the grids is assumed to be energy independent. They might perform better at lower photon energies if the scatter transmission is due to the lead plates which are not thick enough to absorb the incident x rays. However, it was assumed the dominant mechanism for scatter transmission was x rays passing through the interstitial material. The contrast enhancement and relative SNR were calculated

under different scatter fractions and plotted in figures 48 and 49.

Table V. Performance for several commercial grids, measured at a scatter fraction of 85%.¹⁸

Grid ratio	Primary transmission at 69 keV	Scatter transmission at 69 keV
6	0.73	0.27
8	0.64	0.13
12	0.61	0.071

was used. Relative SNR is the SNR normalized by the SNR without any scatter rejection device,

$$k_r^2 = \frac{k^2}{k_0^2} = \frac{C^2}{C_0^2} (FT_s + (1-F)T_p), \quad (18)$$

where k_r is the relative SNR. C and C_0 are the contrast with and without the scatter rejection device, respectively. T_s is the scatter transmission and T_p is the primary transmission of the device.

For most medical x-ray imaging applications, the effective energy ranges from 20 to 70 keV. Mammography has an effective energy of 20 keV. The results in figure 48 show that contrast improvement of all the three hypothetical lenses are better than or as good as that of the three grids. Lens #2 is scaled up from the whole measured lens. This lens has good contrast improvement because of its total scatter rejection. However its relative SNR is lower than that of the grids when the scatter fraction is less than 80% because of its low primary transmission. The primary transmission of this lens is only 33% and the primary transmissions for all the three commercial grids are better than 60%. So with this lens more exposure will be necessary to the patient. Overall primary transmission has to be improved for practical use. Lens#1 is scaled up from the center part of the measured lens. From the calculations, summarized in figures 48 and 49, its performance is significantly better than those of the commercial grids for effective energies of 20-45 keV. This lens will not only improve the contrast in the imaging but also reduce the exposure time to the patient. So it is ideal for mammography.

Assuming that the lead glass capillaries have the same quality as that of borosilicate fibers, we can estimate the performance of a lead glass lens. Simulations of transmission spectra were performed for a source to lens distance of 1.5 m, and the source operated at 120 kVp with a 0.5 mm spot size. For a perfect lens, each channel in the lens is tapered. With a tapered channel, fewer average reflections will be needed for the photons to pass. So theoretically, transmission with a perfect lens is larger than for a straight capillary if they have the same quality. The transmission is quite sensitive to the capillary length. Therefore, as long as the lens has low enough scatter

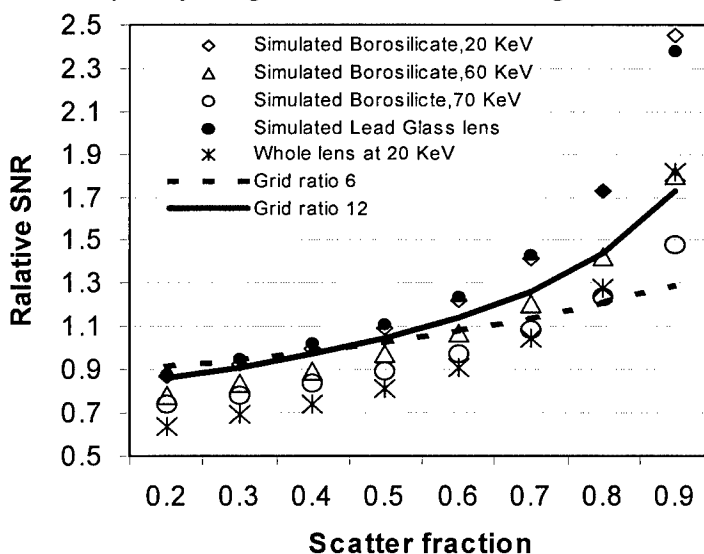


Figure 49. Relative Signal to Noise(SNR) vs. scatter fraction for three hypothetical lenses. The results were compared with the performance of three commercial grids.

transmission, the length of the lens should be kept as short as possible.

The performance estimation results of the lead glass lens in figure 49 are based on the simulated transmission with length of 30 mm. The scatter transmission of this lens is less than 1%.

Primary transmission as high as that of grid is also obtained with simulation. Compared to the grid performance, this lens has higher contrast enhancement and relative SNR.

So this lens will not only improve the contrast of the image, but also reduce the radiation dose to the patient.

5.3.5.3. Leaded Glass Single Fiber Measurements and Analysis

The experimental apparatus for leaded glass single fibers measurements is shown in figures 2 and 3. Description of five types fibers measured and their best fit simulation parameters are listed in Table VI.

Figure 50 shows a source scan plot of transmission of fiber B60 as a function of source location for eight different energy windows of approximately 2 keV in width. The transmission plots are narrower for the higher energy windows, as expected due to the decrease in critical angle with photon energy. For leaded glass fibers, because of the high absorption of lead, the background signal from photons with incidence angle greater than the critical angle is very small. Most of these photons are absorbed rather than cutting through the glass wall. The cut through transmission is 3.6% at 80 keV for a 30-mm-long type B fiber and 0.18% for a 60-mm-long fiber. Measured and theoretical high-angle transmission at several energies are shown in figure 51. The theoretical values are calculated as

$$T_c = \exp \{-L (1-f) \mu \rho \} \quad (19)$$

where L is the fiber length, f is the fractional open area of the fiber, ρ is the density of the glass, and μ is the mass absorption coefficient of the glass obtained from the tabulated values.¹⁹ The transmission results which follow are channel transmissions from which the very small high angle cut through and fluorescence background have been subtracted.

Transmission for leaded glass fibers listed in Table VI was measured in the energy range 9-80 keV. The measured transmission as a function of energy along with the

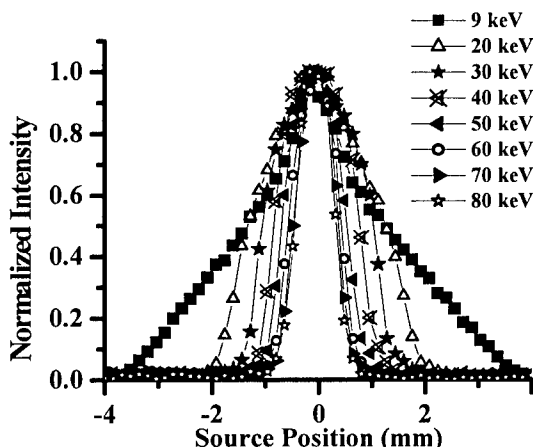


Figure 50. Normalized intensity vs source position, taken by moving the source in the horizontal direction perpendicular to the fiber with fiber and pinhole fixed.

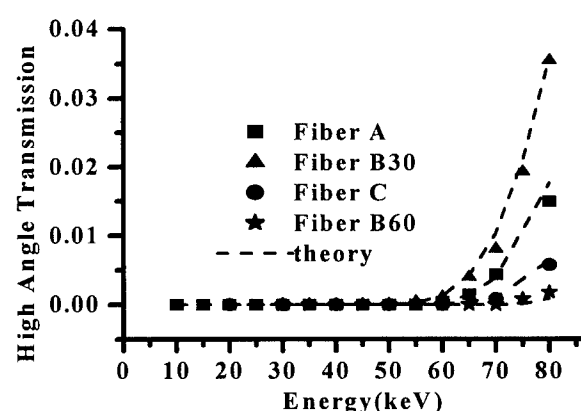


Figure 51. Large angle (cut through) transmission versus energy, measured with the source moved away from the aligned position to an angle larger than the critical angle. Dash lines are theoretical calculation using equation 19.

simulation of different bending radii for type B60 fiber is shown in figure 52. A slight bending can dramatically reduce the transmission at high energies. The simulation with bending alone can not fit the experimental data since at smallest radius the transmission is too high at lower energies and too low at high energies. Bending has very small effect on the transmission at low energies. Since any waviness correction will reduce the transmission, the radius of bend has to be larger than 32 m.

Table VI. Fiber description and simulation parameters

Fiber					Simulation			
Fiber type	Outer diameter mm	Channel size μm	Open area %	Length mm	Bending R m	Waviness w mrad	Layer t μm	Roughness z nm
A	0.53	12	60	60	40	0.26	45	1.8
B30	0.51	12	60	30	30	0.15	18	1.7
B60	0.51	12	60	60	56	0.15	33	1.7
C	0.51	11	50	60	27	0.19	33	1.8
D	0.53	11	50	60	28	0.20	43	1.8
E	0.53	11	40	60	45	0.28	47	2.1

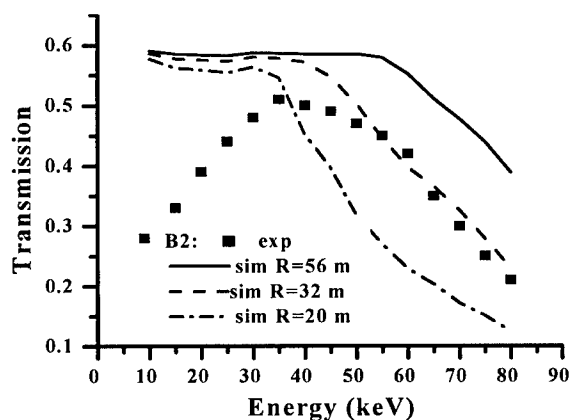


Figure 52. Simulated transmission spectra of a type B60 fiber for different bending radii are compared with the experimental data. The figure shows that bending alone can not fit the data since the smallest bend underestimates the transmission at high energies.

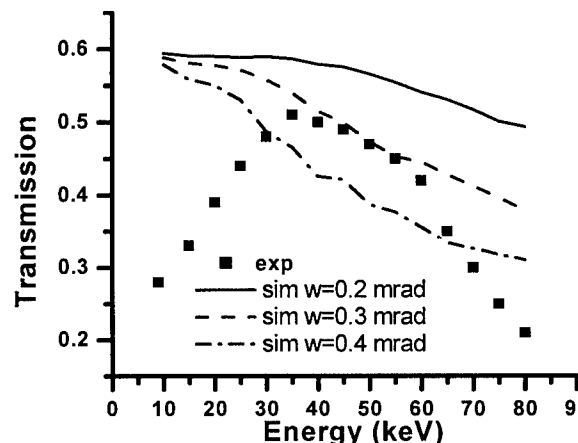


Figure 53. Simulated transmission spectra are compared with the experimental data. The waviness correction causes the transmission to drop primarily in the middle energy range.

Simulations with different waviness corrections are compared to the experimental data of transmission spectra in figure 53. The waviness alone can not fit the data. The simulation shows that the waviness causes the transmission to drop rapidly at medium energies but not rapidly enough at higher energies. Simulated transmission source scans with different waviness are compared to the experimental data at 9 keV in figure 54. The simulation with a waviness of 0.5 mrad fits the spectrum source scan fairly well at 9 keV. However, that was seen to be too large for the transmission spectrum of figure 53. Figure 55 compares the experimental data to simulations at 40 keV, and shows that the maximum value of waviness is 0.15 mrad.

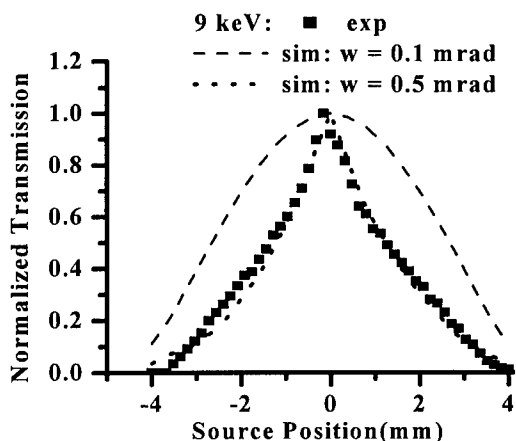


Figure 54. Simulated source scan curves with different waviness are compared with the experimental data at 9 keV. A waviness of 0.5 mrad, which is too large at higher energies, is needed to fit the data.

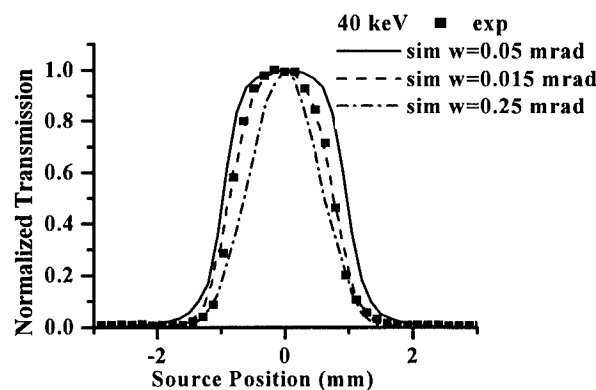


Figure 55. Simulated source scan curves with different waviness are compared with the experimental data at 40 keV. Since the simulated curve with a waviness of 0.15 mrad fits the data fairly well, it is used as the value for waviness in the best fit simulation parameters in Table VI.

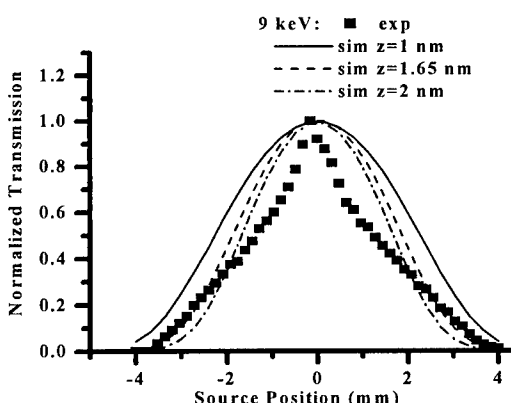


Figure 56. Simulated source scan curves for a type B60 fiber for different roughness are compared with experimental data at 9 keV. The curve is too low at large displacements for the highest value of roughness.

The roughness has only a fairly small effect on the transmission spectrum. The simulated transmission source scan curves with different roughnesses compared with the experimental data at 9 keV is shown in figure 56. The transmission at high angles is sensitive to roughness. The transmission is too small if the roughness is larger than 1.7 nm.

By modeling channel blockage with a glass filter layer of thickness t , the simulated transmission spectrum with the glass layer alone fits the data at low energies. The simulated transmission spectra with different layer thicknesses are compared with the experimental data in figure 57. The simulated transmission with best fit simulation parameters, which with

and without including glass inclusions with a thickness of 33 μm compared with the data for type B60 fiber is shown in figure 58. As shown in figure 58, the inclusion of a 33 μm thick leaded glass layer gives a good fit with the experimental transmission spectrum.

The best fit simulation compared to the experimental source scan curves are shown in figures 59-62. The simulated transmission source scan curves fit the data fairly well at energies from 20 to 80 keV. The source scan at 9 keV does not fit the simulated transmission, as shown in figure 59. This may be partly because the actual value of the transmission at 9 keV, as shown in figure 58, is quite low.

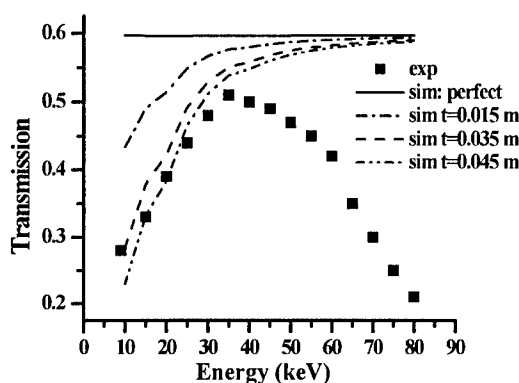


Figure 57. Simulated transmission with different layer thicknesses alone compared with experimental data. The figure shows that the maximum layer thickness for a type B60 fiber is 35 μm to fit the low energy transmission.

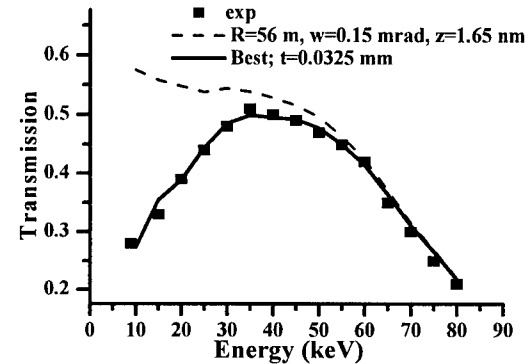


Figure 58. Simulated transmissions with and without leaded glass filter for type B60 fiber are compared with the experimental data. Best fit is simulated transmission with $R=56$ m, $w=0.15$ mrad, $z=1.7$ nm, and $t=33$ μm .

The primary effect of bending is to reduce the transmission at high energies. Channel blockage reduces the transmission at low energies. Roughness reduces the width of source scan at low energies. Waviness primarily reduces the transmission and the source scan width at mid range energies.

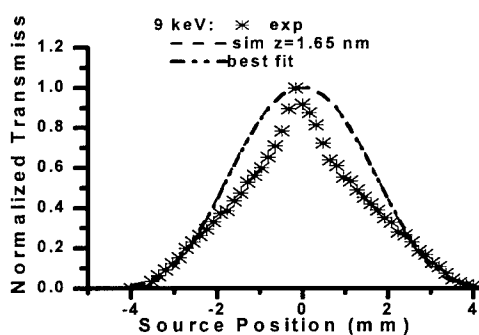


Figure 59. Simulation of source scan curves with $z=1.7$ nm, $R=56$ m, and $w=0.15$ mrad, and with roughness $z=1.7$ nm alone, compared with the experimental data. Since the actual transmission at this energy is quite low, the source scan curve might be somewhat distorted, and thus the simulation does not fit the data well.

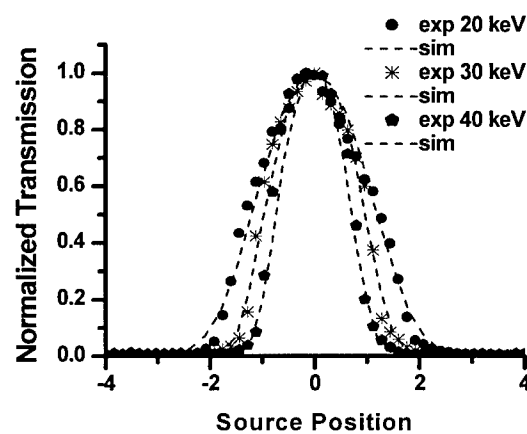


Figure 60. Simulated scan curves compared with the experimental data at three photon energies.

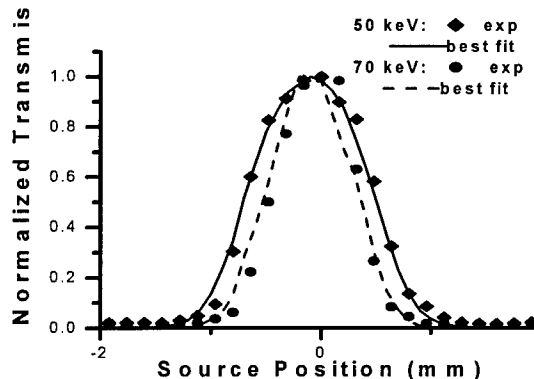


Figure 61. The simulation of scan curves with best fit parameters at 50 and 70 keV, compared with the experimental data.

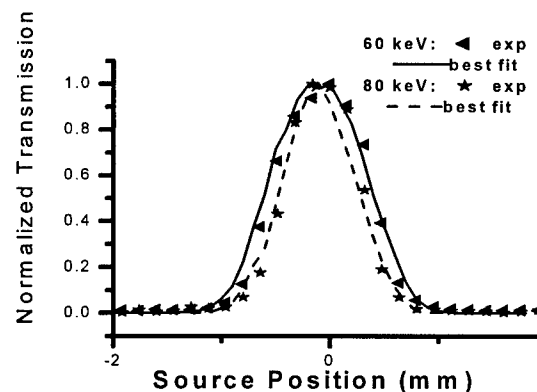


Figure 62. The simulation of scan curves with best fit parameters at 60 and 80 keV, compared with the experimental data.

The best fit simulated transmissions along with the experimental data are shown in figures 50 and 51.^{20,21} The outer diameter of the fibers are in the 0.51- 0.53 mm range. The fractional open area of the fibers range from 60% to 40%. These fibers are thin and flexible, and therefore are difficult to keep straight in the measurement apparatus, resulting in sharp bending radii and relatively poor high-energy transmission.

Fiber type B has high open area, low channel blockage, and the least bending and waviness. Thus this fiber has better transmission than the other fibers. Figure 63 shows that the transmission of this fiber type with a shorter length (B30) is higher at lower energies because of its thinner blockage layer. This is consistent with a statistically random model of glass inclusion. Because of its high flexibility, the shorter fiber experiences more bending than the longer ones, and thus the transmission falls off faster at higher energies. The shorter fiber has a higher scatter cut through, as shown in

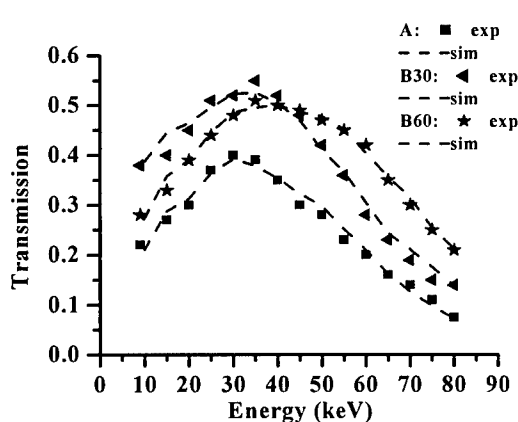


Figure 63. Simulation of transmission spectra of fiber A, fiber B60 (B with length of 60 mm) and fiber B30 (B with length of 30 mm) with their best fit parameters listed in Table VI, compared with the experimental data.

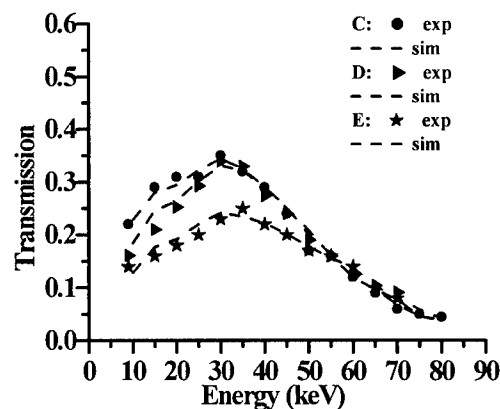


Figure 64. Simulated Transmission spectra of fiber C, fiber D and fiber E with their best parameters listed in Table VI, compared with the experimental data.

figure 51. The different open area, bending, waviness and blocked channels cause the differences in the transmission among the fibers. Fiber type C and D have the same open area, but fiber type C has thinner glass layer, as listed in Table VI. As a result, fiber type C has higher transmission at lower energies than fiber type D, as shown in figure 64.

The high measured transmission (>42%) for fiber type B shows that the performance of this leaded glass fiber is quite good in the 20-50 keV energy range. The geometric simulation, with roughness, waviness, bending and channel blockage corrections, performs well in explaining the measured transmission spectra above 15 keV. According to this simulation, bending is the most harmful at higher energies, and glass inclusions that block the channels are harmful at lower energies. For type B fibers, even though the roughness is high, the waviness is low and the bending radius is the largest among the fibers. The high-energy transmission performances could be improved by making the fiber diameter larger and therefore more rigid to minimize unintentional bending. Low energy performance is improved by using shorter fibers. Because of the good absorption of lead, the high-energy photons, which are not reflected, are absorbed completely by 60 mm-long fibers, even at 80 keV. The high-angle transmission at 80 keV is only 0.2%. A shorter fiber, which is 30 mm in length has a transmission efficiency more than 40% at 20 keV and scatter transmission of 3.6% at 80 keV. This high-angle transmission is very much less than the 16% for a longer (140 mm) borosilicate fiber. Thus short leaded glass polycapillary x-ray optics are very promising for scatter rejection in mammography applications.

6 Key Research Accomplishments

- Development of extensive modeling capability for polycapillary optics that includes realistic models for the effects of profile defects and shows extremely good agreement with measured data and therefore the capability to predict performance in new geometries.
- Measured polycapillary fiber transmission in excess of 65% at 20 keV for borosilicate glass. Measured high angle transmission (which corresponds to scatter transmission) is lower than 1% for 12 cm long borosilicate glass optics.
- Modeling, measurement and defect studies have led to better manufacturing capabilities for magnifying tapered monolithic optics. These optics have demonstrated the ability to provide nearly ideal scatter rejection and contrast enhancement, while at the same time increasing the system MTF performance at all spatial frequencies. A multitaper optic has been produced and tested.
- Image analysis studies have provided the means for image artifact analysis and reduction.
- Measured leaded glass polycapillary fiber transmission is in excess of 45% at 20 keV. Measured high angle transmission is less than 4% for a 30 mm long fiber at 80 keV.

7 Reportable Outcomes

7.1 Manuscripts

Lei Wang, C. A. MacDonald, and W. W. Peppler, "Performance of Polycapillary Optics for Hard X-ray Imaging," accepted, *Medical Physics*.

Lei Wang, W.M. Gibson, C.A. MacDonald, "Potential of Polycapillary X-Ray Optics in Medical Imaging Applications," in C.A. MacDonald, K.A. Goldberg, J.R. Maldonado, A.J. Marker III, S.P. Vernon, eds., **EUV, X-ray, and Neutron Optics and Sources**, SPIE vol. 3767, 1999.

S.D. Padiyar, M.V. Gubarev, Hui Wang, W.M. Gibson, C.A. MacDonald "Characterization of Polycapillary X-Ray Collimating Optics", in C.A. MacDonald, K.A. Goldberg, J.R. Maldonado, A.J. Marker III, S.P. Vernon, eds., **EUV, X-ray, and Neutron Optics and Sources**, SPIE vol. 3767, 1999.

S.D. Padiyar, H. Wang, W.M. Gibson, C.A. MacDonald, M.V. Gubarev, "Beam Collimation Using Polycapillary X-Ray Optics For Large Area Diffraction Applications," in **Advances in X-ray Analysis**, 43, Proceedings of the 48th Denver X-ray Conference, 1999.

Hui Wang, Lei Wang, W.M. Gibson, C.A. MacDonald, "Simulation Study of Polycapillary X-Ray Optics," in **X-Ray Optics, Instruments, and Missions**, R.B. Hoover and A.B.C. Walker II, eds. SPIE Vol 3444, pp. 643-651, July 1998.

B.K. Rath, W.M. Gibson, Lei Wang, B.E. Homan and C.A. MacDonald, "Measurement and Analysis of Radiation Effects in Polycapillary X-ray Optics," *Journal of Applied Physics*, 83, no.12, pp. 7424-7435, June 15 1998.

Suparmi,Cari, W.M. Gibson, C.A. MacDonald, "Development of Polycapillary X-Ray Optics for Scatter Rejection," in **Advances in Laboratory-Based X-Ray Sources and Optics**, SPIE Vol. 4144, 2000.

Suparmi, Cari, Lei Wang, Hui Wang, W.M. Gibson, C.A. MacDonald, "Measurement and Analysis of Leaded Glass Polycapillary Optic Performance for Hard X Rays," to be submitted for *Journal of Applied Physics*.

Cari, Suparmi, S.D. Padiyar, W.M. Gibson, C.A. MacDonald, C.D. Alexander, M.K. Joy, C.H. Russel, Z.W. Chen, "Characterazation of a Long Focal Length Polycapillary Optic for High Energy X Rays," in **Advances in Laboratory-Based X-Ray Sources and Optics**, SPIE Vol. 4144, 2000.

7.2 Presentations

Lei Wang, W.M. Gibson, C.A. MacDonald, "Potential of Polycapillary X-Ray Optics in Medical Imaging Applications," SPIE 1999.

Suparmi, Cari, W.M. Gibson, C.A. MacDonald, "Development of Anty Scatter Optics Using Leaded Glass Polycapillary," SPIE 2000.

7.3 Poster Presentations

Hui Wang, Lei Wang, W.M. Gibson, C.A. MacDonald, "Simulation Study of Polycapillary X-ray Optics," SPIE San Diego 7/98.

Suparmi, Cari, W.M. Gibson, C.A. MacDonald, "Measurement and Analysis of Leaded Glass Polycapillary Optics for Mammography," Era Hope Meetings, Atlanta, 2000.

7.4 Employment/Research Received

7.4.1 RESEARCH EMPLOYMENT

Lei Wang, Postdoctoral Residency, University of California at San Francisco, 1999.

8 Conclusions

Some manufacturing problems have occurred with scaling up the optics to clinical size. These problems have been addressed by the studies of defect properties. Notwithstanding the problems, the optics tested have performed extremely well. Multifiber collimating optics and monolithic linear magnifying tapers have been studied. Scatter rejection is very high from all the optics. The linear tapers resulted in nearly ideal contrast enhancements and simultaneously increase in MTF at all spatial frequencies. This will result in an improvement in resolution regardless the inherent spatial resolution of the detector. The rapidly growing modeling capability has lead to a real development of understanding of the nature of polycapillary defects, which has lead to improvements in the manufacturing processes. Further, the increased confidence in the modeling allows future lens geometries to be effectively "tested" in simulation so that design parameters can be rapidly optimized. Short leaded glass polycapillary optics which have good transmission at mammographic energies provide excellent for scatter rejection.

9 References

¹ M.A. Kumakhov, F.F. Komarov, "Multiple Reflection from Surface X-Ray Optics," *Physics Reports*, **191**, (5): p. 289-350, 1990.

² W. M. Gibson, C. A. MacDonald and M. A. Kumakhov, "The Kumakhov Lens: A New X-ray and Neutron Optics with Potential for Medical Applications", in **Technology Requirements for Biomedical Imaging**, (ed. S. K. Mun, R. von Hanwehr and P. Gerity), IEEE Proc. 2580, 164-169 (1991).

³ J.F. Butler, F.P. Doty, B. Apotovsky, J. Lajzerowicz and L. Verger, "Gamma-and-X-ray detectors manufactured from $Cd_{1-x}Zn_xTe$ grown by a high pressure Bridgman method", *Materials Science & Engineering*, B16, 291 (1993).

⁴ M. Singh, F.P. Doty, S.J. Friesenhahn, J.F. Butler, "Feasibility of using cadmium-zinc-telluride detectors in electronically collimated SPECT." (Selected papers from the 1994 Nuclear Science Symposium and Medical Imaging Conference (NSS/MIC)), *IEEE Transactions on Nuclear Science*, August 1995, v42, n4, p1139(8).

⁵ Carman Abreu, "Investigation of Capillary Optics for Potential Use in Mammography", thesis for Ph.D. in physics, University at Albany, 1994.

⁶ David G. Kruger, Carmen C. Abreu, Eric G. Hendee, Armen Kocharian, Walter W. Peppler, Charles A. Mistretta and Carolyn A. MacDonald, "Imaging characteristics of x-ray capillary optics in digital mammography," *Medical physics*, Vol. 23, No. 2, Feb. 1996, pp 187-196.

⁷ Q.F. Xiao, I.Y. Ponamarev, A.I. Kolomitsev and J.C. Kimball, in R.B. Hoover, ed., **X-ray Detector Physics and Applications**, SPIE 1992.

⁸ B.L. Henke, E.M. Gullikson, and J.C. Davis, *Atomic Data and Nuclear Data Tables*, **54** (2), p. 181, 1993.

⁹ Lei Wang, B.K. Rath, W.M. Gibson, J.C. Kimball, C.A. MacDonald, "Measurement and Analysis of Capillary Optic Performance for Hard X rays", *Jour. Appl. Phys.*, September 15, 1996.

¹⁰ Hui Wang, Lei Wang, W.M. Gibson, C.A. MacDonald, "Simulation Study of Polycapillary X-Ray Optics," in SPIE Vol 3444, July 1998.

¹¹ Lei Wang and C.A. MacDonald, "Measurement of Capillary Optic Performance for Hard X rays," in R.B. Hoover and M.B. Williams, **X-ray and Ultraviolet Sensors and Applications**, SPIE vol. 2519, July 1995.

¹²Lei Wang and C.A. MacDonald, "Measurement and analysis of capillary optic performance for hard x-rays", **Hard X-ray/Gamma-Ray and Neutron Optics, Sensors, and Applications**, R.B. Hoover, and F.P. Doty, eds., SPIE Proceedings Vol. 2859.

¹³ J.C. Kimball and D. Bittel, "Surface Roughness and Scattering of glancing angle x-rays: Applications to X-ray lenses" *J. Appl. Phys.*, **74** (2), 15 July 1993.

¹⁴ Qin-sheng Chen, Michel Defrise, and F. Deconinck, "Symmetric Phase-Only Matched Filtering of Fourier-Mellin Transforms for Image Registration and Recognition", *IEEE Transactions on Pattern Analysis and Machine Intelligence*, Vol. 16, No. 12, December, pp. 1156.

¹⁵ Hiroshi Fujita, et. al. "A Simple Method for Determining the Modulation Transfer Function in Digital Radiography", *IEEE Transaction on Medical Imaging*, Vol. 11, No. 1, pp. 34.

¹⁶ Ehsan Samei, Michael J. Flynn, David A. Reimann, "A Method for Measuring the Presampled MTF of Digital Radiographic Systems using an Edge Test Device", manuscript submitted to *Medical Physics*, 1996.

¹⁷ John M. Boone and Seibert, "An analytical edge spread function model for computer fitting and subsequent calculation of the LSF and MTF", *Medical Physics*, Vol. 21, No. 10. October 1994., pp.1541

¹⁸ C. E. Dick and J. W. Motz, "New method for experimental evaluation of x-ray grids", *Medical Physics*, Vol. 5, No. 2, Mar./Apr. 1978.

¹⁹The NNDC online data service, Brookheaven National Lab Nuclear Data Center. (Remote host address: bnlnd2.dne.bnl.gov.)

²⁰Suparmi,Cari, W.M. Gibson, C.A. MacDonald, "Development of Polycapillary X-Ray Optics for Scatter Rejection," in **Advances in Laboratory-Based X-Ray Sources and Optics**, SPIE Vol. 4144, 2000.

²¹Suparmi, Cari, Lei Wang, Hui Wang, W.M. Gibson, C.A. MacDonald, "Measurement and Analysis of Leaded Glass Polycapillary Optic Performance for Hard X Rays," to be submitted for *Journal of Applied Physics*.

10 APPENDICES

10.1 BIBLIOGRAPHY

Investigator' s Name : Suparmi

Part time Post Doctoral Student in Physics, University at Albany, State University of New York

EDUCATION

Ph D in Theoretical Physics (Supersymmetric in Semi Classical Quantum Mechanics) University at Albany, State University of New York (May 1992)

MA in Theoretical Physics, The College at New Paltz, State University of New York (May 1988)

Dra in Physics Education, Institute of Education and Teacher Training, Jogyakarta (May 1981)

BA with honor in Physics, Institute of Education and Teacher Training, Surakarta (June 1975)

POSITION HELD

Center for X-Ray Optics, University at Albany, State University of New York

Part time Post Doctoral Researcher (June 1988-August 1999)

Research Associate (Sept 1997- May 1998).

Full time Post Doctoral Researcher (August 1999- September 2000)

MEASUREMENT AND ANALYSIS OF LEADED GLASS POLYCAPILLARY OPTIC PERFORMANCE FOR HARD X RAYS

Suparmi, Cari, Lei Wang,^{*} Hui Wang, W.M. Gibson, C.A. MacDonald

Center for X-ray Optics, University at Albany, State University of New York, Albany, NY 12222

^{*} Currently at UCSF

1. ABSTRACT

The properties of borosilicate glass single polycapillary optics have been previously studied in 10-80 keV energy range. However, many medical imaging and industrial applications for x rays require large area optics with good scatter rejection. Since shorter optics are easier to manufacture, optics with a shorter length would provide a faster route to bringing the benefit of polycapillary optics to these applications. Leaded glass would allow the optic to be much shorter and still give good contrast enhancement, because of the superior absorption of leaded glass. In order to investigate the feasibility of using leaded glass polycapillary optics for these applications, measurements and simulations have been performed on the behavior of leaded glass polycapillary fibers in the 9-80 keV energy range. These fibers have outer diameter about 0.5 mm, channel diameter of 12 μm and open area from 40% to 60%. The transmission efficiencies of these fibers of different types and lengths were measured as a function of source location and x-ray energy. The measurements were analyzed using a geometrical optics simulation program, which included roughness, waviness, bending effects and a leaded glass filter layer. Despite low transmission at low energies, leaded glass polycapillary optics with a length of 30-60 mm seem promising for many high energy (>20 keV) x-ray applications. Type B fibers

60 mm in length have transmission efficiency of 50% in the 35-40 keV energy range, which is 83% of fiber's open area, and very low scatter transmission of 0.18% at 80 keV. The same fiber with the shorter length of 30 mm has higher transmission at lower energies, and more than 52% in the 20- 40 keV energy range.

2. INTRODUCTION

Polycapillary optics, consisting of arrays of tiny hollow glass tubes with diameters on the order of few microns, is a relatively new technology for controlling x-ray beams. A polycapillary fiber is a capillary bundle with hundreds or thousands of hollow channels, as shown in figure 1. X rays striking the interior of the glass tubes at grazing incidence are guided down the tubes by total external reflection. Arrays of curved or tapered capillaries can be used to focus, collimate and filter x-ray radiation. Polycapillary optics have potential usefulness in many applications, including x-ray lithography, medical imaging, crystallography and astronomy.¹⁻⁹ Properties of borosilicate polycapillary fibers, fabricated optics, and their applications have been studied extensively in the 8-80 keV energy range.¹⁰⁻¹⁵ Leaded glass fiber optics are advantageous for excellent scatter rejection compared to borosilicate glass fibers because of their superior absorption.

In this paper, measurement results for variety of leaded glass single fibers in the energy range from 9 to 80 keV are presented. The results were analyzed using a geometrical optic simulation program. The use of the simulation to analyze the experimental data from 60 mm long type B fibers is demonstrated. Finally, the fitting processes were used to determine the best fit parameters of the simulation for five other leaded glass fibers. The measurements show the potential for applications at energies from 25 to 80 keV for short length optics. The analyses from the simulation indicate that waviness and bending are harmful to the transmission at higher energies, and partially blocked channels are more harmful for lower energies.

3. BASIC PRINCIPLE

Capillary x-ray optics use multiple total external reflection to guide grazing incidence x rays in arrays of tiny hollow glass tubes. X-ray photon energies are much larger than the plasma energies of glasses, which are tens of electron volts. In this regime, the real part of refractive index of glass can be simply approximated by¹⁶

$$n^2 = \epsilon / \epsilon_0 = 1 - (\omega_p^2 / \omega^2) \quad (1)$$

where n is the index of refraction of glass, ϵ is the dielectric constant of the glass, ω is the x-ray frequency, ω_p is the plasma frequency of the glass, and ϵ_0 is the dielectric constant for vacuum. The plasma frequency ω_p for leaded glass is small compared to the photon frequency, so that n is slightly less than unity. Therefore, total external reflection can occur at the air to glass interface. Using Snell's Law, the critical grazing angle θ_c can be found from

$$\sin(\frac{\pi}{2} - \theta_c) = n \times \sin(\frac{\pi}{2}). \quad (2)$$

Therefore,

$$\theta_c = \omega_p / \omega \quad (3)$$

For leaded glass capillaries that were used in the experiments described here, the critical angle for reflection is

$$\theta_c = 35 \text{ (mrad)} / E \text{ (keV)} \quad (4)$$

The higher the photon energy, the smaller is the critical angle.

4. GEOMETRIC SIMULATION

In the geometrical optic simulation used in this article, x-ray transmission through hollow glass fibers is simulated by tracing a large number of x rays through fibers. The simulation includes four fiber quality defects: roughness; waviness; channel blockage; and also profile corrections that can be approximated by uniform bending. It had been shown previously that geometric simulations with these four best parameters are in good agreement with experimental data for borosilicate single fibers at 1- 80keV.^{13,17}

The geometric algorithm is a two dimensional approximation. Because of the small critical angle, the velocity of the x-ray photon along the capillary axis is nearly equal to c , the velocity of light. The trajectory of an x-ray can be reduced to the two dimensional motion inside the capillary cross section.¹³ Deviations of the channel from a straight path are approximated by uniform bending described by a bending radius, R . The bending of the channel make the apparent motion of the x ray within the channel cross section similar to that of a classically accelerated particle.

Surface roughness is formally parameterized by a correlation length and root-mean square displacement of rough surface, z . Because changes in the correlation length change the effective roughness height, and due to the lack of actual correlation data, the correlation length was fixed at 6 μm for all simulations. Changing this value would cause a proportional scaling all of reported roughness heights. The value was chosen for borosilicate fibers so that the roughness heights agree with atomic force microscopy data.¹³ The surface roughness decreases the apparent reflectivity of the channel walls and therefore

the transmission in capillary channels. The third capillary surface quality parameter is waviness, which occurs on a spatial range shorter than the capillary length and longer than roughness. The average effect of the waviness can be considered as a random tilt of glass wall. The maximum random tilt angle w is an adjustable parameter. In the simulation, these tilt angles are normally distributed with a mean value of zero and a standard deviation w . The fourth polycapillary defect is channel wall blockage, which is modeled by a filter layer of glass of thickness t . The layer represents glass inclusions which randomly occur along the fiber.

5. EXPERIMENTAL APPARATUS AND TECHNIQUE

5.1 Experimental Apparatus

The experimental apparatus is shown in figure 2.

5.1.1. Source

The x-ray generator used in the experiment was a low current Microfocus MS50 with a 50 μm spot size, tungsten target, and a maximum operating voltage of 100 kVp. The source head was mounted on a stage which could be moved in the two directions transverse to the x-ray beam. In order to reduce the background of scattered x rays, this movable source was enclosed in a 6-mm-thick lead box with a 100x175 mm aperture in the front. The source to fiber distance was 1100 mm. In the measurement for photons with energy higher than 50 keV, a 5-mm-thick aluminum plate was used as a filter between the source and the fiber to remove the low energy photons, and reduce the dead time of detector.

5.1.2. Pinhole

A 200 diameter pinhole through 4 mm of lead, 2 mm tungsten, and 1 mm of tantalum (attached together), was placed 5mm away from the fiber at the entrance end. The pinhole was attached to a 6-mm-thick lead shield. The pinhole and lead shield together block scattered x rays and leakage around the outside of the fiber. The pinhole was smaller than the fiber but still covers hundreds or more channels. Its small size was chosen not only to avoid the leakage around the fiber and reduce dead time in the detector, but also to keep the source-fiber distance as small as possible while keeping the photon entrance angle at the edges of the pinhole to less than the critical angle at energies up to 80 keV.

5.1.3. Fiber

The fiber was held straight by a finely machined groove in an aluminum plate and covered by iron powder to prevent x-ray leakage around the fiber. The aluminum plate was also mounted on a stage which can be translated in two orthogonal directions transverse to the beam. All stages were mounted on rail carriers which could be moved along the beam directions. Five kinds of fibers, listed in Table I, were measured. The outer cross sections of all five fibers are roughly hexagonal.

5.1.4. Detector

The detector was a high purity germanium detector with about 200 eV resolution at 5.9 keV and 550 eV at 122 keV. The detector was placed behind the fiber. The distance between the source and detector was fixed to keep air absorption constant. Motion control and data collection were all controlled with a small computer.

6. MEASUREMENT RESULTS AND ANALYSIS

6.1. High Angle Transmission

The pinhole was located in the center of the fiber to avoid leakage. Figure 3 shows a source scan plot of transmission as a function of source location for seven different energy windows of approximately 2 keV in width. The transmission plots are narrower for the higher energy windows, as expected due to the decrease in critical angle with photon energy. For leaded glass fibers, because of the high absorption of lead, the background signal from photons with incidence angle greater than the critical angle is very small. These photons are absorbed, rather than cutting through the glass wall. The cut through transmission is 3.6% at 80 keV for a 30-mm-long type B fiber and 0.18% for a 60-mm-long fiber. Measured and theoretical high-angle transmission at several energies are shown in figure 4. The theoretical values are calculated using

$$T_c = e^{-\ell(1-f)\mu\rho} \quad (5)$$

where ℓ is the fiber length, f is the fractional open area of the fiber, ρ is the density of the glass, and μ is the attenuation coefficient of the glass obtained from the tabulated values.¹⁸ The transmission results which follow are channel transmissions from which the very small high angle cut through and fluorescence background have been subtracted.

6.2. Simulation Analysis

Transmission for the leaded glass fibers in Table I was measured in the energy of 9- 80keV. To illustrate the effect of each simulation parameter, the application of the simulation to the experimental data for fiber type B60 (a 60mm-long type B fiber) is discussed in this section.

6.2.1. Bending effects

A slight bending can dramatically reduce the transmission at the high energies because of the small critical angles. The measured transmission as a function of energy along with the simulations with different bending radii for fiber type B60 is shown in figure 5. The simulation with bending alone can not fit the experimental data since at smallest radius the transmission is too high at lower energies and too low at high energies. Since any waviness correction will reduce the transmission, the radius of bending has to be larger than 32 m. Simulations with different bending radii and the experimental transmission source scan at 9 keV are shown in figure 6. Even with a sharp bend, the simulated transmission source scan at 9 keV is not narrow enough. Thus additional corrections are necessary.

6.1.2. Waviness effects

Simulations with different waviness corrections are compared to the experimental data of transmission spectra for a type B60 fiber in figure 7. The waviness alone can not fit the data. The simulation shows that the waviness causes the transmission to drop rapidly at medium energies but not rapidly enough at higher energies. Figure 7 shows that the waviness correction has to be smaller than 0.3 mrad to fit the data. Simulated transmission source scans with different waviness are compared to the experimental data at 9 keV in figure 8. The simulation with a waviness of 0.5 mrad fits the spectrum source scan fairly well at 9 keV. However, that was seen to be too large for the transmission spectrum of figure 7. Figure 9 compares the experimental data to the simulations at 40 keV, and shows that the maximum value of waviness is 0.15 mrad.

6.2.3. Roughness effects

Simulation of the transmission of fiber type B60 with and without roughness corrections are compared to the experimental data in figure 10. For a perfect capillary, the transmission spectrum is flat, since the distance between the source and the fiber is large enough to ensure that every photon which hits the glass wall has grazing angle smaller than its critical angle. The transmission is almost flat at all energies, but for high roughness drops more rapidly at medium energies than at high energies. The transmission drop depends on both the surface reflectivity, which is reduced by roughness, and the number of reflections that the photon undergoes through the channel. The transmission is proportional to R^n where R is reflectivity, and n is the number of bounces. For a straight capillary, the average number of bounces of the photon along the channel is small, usually less than three. Thus the roughness has only fairly small effect on the transmission spectrum. The transmission as a function of source location at 9 keV is shown in figure 11. Because photons experience more than 21 reflections for large source displacements, the transmission at high angles is sensitive to roughness and becomes too small if the roughness is larger than 1.7 nm.

6.2.4. Channel blockage

The drop in transmission at low energies can be fit by modeling channel blockage with a glass filter layer of thickness t . The simulated transmission spectra with different layer thicknesses is compared with the experimental data in figure 12. The simulated transmission spectrum with a glass layer thickness of 35 μm alone fits the data type B60 fiber at low energies. To fit the high energy transmission spectrum data, finally, we combine the waviness determined from source scan curve at 40 keV, the roughness determined from source scan curve at 9 keV, and add the bending radius. To fit low

energy transmission, then the simulation result must include absorption by a leaded glass layer determined from figure 12, which must be less than 35 μm . Figure 13 shows that the inclusion of a 33 μm thick glass layer gives a good fit with the experimental transmission spectrum.

The simulation with the four best fit simulation parameters is compared to the experimental source scans in figures 14-17. The simulated transmission source scan at medium and high energies fits the data fairly well. The source scan at 9keV does not fit the simulated transmission, as shown in figure 14. This may be partly because the actual value of the transmission at 9 keV, as shown in figure 13, is quite low.

6.2.5 Simulation summary

The primary effect of bending is to reduce the transmission at highest energies. Channel blockage reduces the transmission at lowest energies. Roughness reduces the width of source scan width at these low energies. Waviness reduces the transmission and the source scan at mid range energies.

6.3. Explanation Experiment Results

Using the fitting processes described in section 6.2, the best fit simulation parameters for fibers A, C, B60, D and E, which have length 60 mm, and also fiber B30, which has length 30 mm, were obtained. The best fit simulation parameters are listed in Table I. The best fit simulated transmissions along with the experimental data are shown in figures 18 and 19. The outer diameter of the fibers are in the 0.51- 0.53 mm range. These fibers are thin and flexible, and therefore are difficult to keep straight in the measurement apparatus, resulting in sharp bending radii and relatively poor high-energy transmission.

Fiber type B has high open area, low channel blockage, and the least bending and waviness. Thus this fiber has better transmission than other fibers. Figure 18 shows that the transmission of this fiber type with the shorter length (B30) is higher at lower energies because of its thinner blockage layer. This is consistent with a statistically random model of glass inclusion. Because of its high flexibility, the shorter fiber experiences more bending than the longer fiber, and thus the transmission falls off faster at higher energies. The shorter fiber has a higher scatter cut through, as shown in figure 4. The differences in the transmission among the fibers are caused by the different open area, bending, waviness and blocked channels. Fiber type C and D have the same open area, but fiber type C has thinner glass layer. As a result, fiber type C has higher transmission at lower energies than fiber type D, as shown in figure 19.

7. CONCLUSIONS

The high measured transmission (>45%) for fiber type B shows that the performance of this leaded glass fiber B is quite good in the 25-50 keV energy range. The geometric simulation, with roughness, waviness, bending and channel blockage corrections, performs well in explaining the measured transmission spectra above 15 keV. According to this simulation, bending is the most harmful at higher energies, and glass inclusions that block the channels are harmful at lower energies. For type B fibers, even though the roughness is high, the waviness is low. The bending radius is the largest among the fibers. The high-energy transmission performances could be improved by making the fibers larger in diameter and therefore more rigid to minimize an unintentionally bending. Low energy performance is improved by using shorter fibers. Because of the good absorption of lead,

the high-energy photons which are not reflected are absorbed nearly completely by 60 mm-long fibers, even at 80 keV. The high angle transmission at 80 keV is only 0.2%. At energies below 50 keV, the high angle transmission is negligible for the 30 mm length. Thus short leaded glass polycapillary x-ray optics are very promising for scatter rejection applications.

8. AKNOWLEDGEMENT

The authors wish to acknowledge assistance from Michael Gubarev, Frank Hoffman, Christine Russel, C.A. Freinberg-Trufas, Francisca Sugiro and Sushil Padiyar. This work was supported by the Department of Army Breast Cancer Research Project grant DAMD17-97-1-7304, and NIH grants.

9. REFERENCES

¹ W. M. Gibson, C. A. MacDonald and M. A. Kumakhov, " The Kumakhov Lens: A New X-ray and Neutron Optics with Potential for Medical Applications", in **Technology Requirements for Biomedical Imaging**, S. K. Mun, R. von Hanwehr and P. Gerity, eds., IEEE Proc. 2580, 164-169 (1991).

²C.A. MacDonald, "Applications and Measurements of Polycapillary X-Ray Optics," *Journal of X-Ray Science and Technology*, **6**, pp. 32-47, 1996.

³D.G. Kruger, C.C. Abreu, E.G. Hendee, A. Kocharian, W.W. Peppler, C.A. Mistretta, C.A. Macdonald, "Imaging Characteristic of X-Ray Capillary Optics in Mammography," *Medical Physics* **23**, (2), pp. 187-196, February 1996.

⁴C.C. Abreu and C.A. MacDonald, "Beam Collimation, Focusing, Filtering and Imaging with Polycapillary X-Ray and Neutron Optics," invited review article, *Physics Medica*, vol. **XIII**, N. 3,

pp. 79-89, 1997.

⁵C.A. MacDonald, S.M. Owens, and W.M. Gibson, "Polycapillary X-Ray Optics for Microdiffraction," *Journal of Applied Crystallography*, **32**, pp. 160-7, 1999.

⁶S.M. Jorgensen, D.A. Rayes, C.A. MacDonald, E.L. Ritman, "Micro-CT Scanner With a Focusing Polycapillary X-Ray Optic," in **Developments in X-Ray Tomography II**, U. Bonse, ed., SPIE vol. 3772, pp. 158-166, 1999.

⁷F.A. Hofmann, W.M. Gibson, C.A MacDonald, D.A. Carter, J.X. Ho, J.R. Ruble, "Complete Data Sets Acquired with Different Polycapillary X-Ray Optic-Source Configurations," in **Advances in X-Ray Analysis**, 43, Proceedings of the 48th Denver X-Ray Conference, 1999.

⁸C.H Russel, M. Gubarev, J. Kolodziejczak, M. Joy, C.A. MacDonald, and W.M. Gibson, "Polycapillary X-Ray Optics for X-Ray Astronomy," in **Advance in X-Ray Analysis**, 43, Proceedings of the 48th Denver X-Ray Conference, 1999.

⁹Lei Wang, C. A. MacDonald, and W. W. Peppler, "Performance of Polycapillary Optics for Hard X-ray Imaging," accepted, *Medical Physics*.

¹⁰C.A. MacDonald, C.C. Abreu, S. Budkov, H. Chen, X. Fu, W.M. Gibson, Kardiawarman, A. Karnaukhov, V. Kovantsev, I. Ponomarev, B.K. Rath, J.B. Ullrich, M. Vartanian, Q. F. Xiao, "Quantitative Measurements of the Performance of Capillary X-Ray Optics", in **Multilayer and Grazing Incidence X-Ray/EUV Optics II**, R.B. Hoover and A. Walker, eds., SPIE Proc. vol. 2011, pp. 275-286, 1993.

¹¹J.B Ullrich, V. Kovantsev, C.A. MacDonald, "Measurements of Polycapillary X-Ray Optics", *Jour. Appl. Phys.*, **74** (10), Nov. 15, pp. 5933-5939, 1993.

¹²C.C. Abreu, D.G. Kruger, C.A. MacDonald, C.A. Mistretta, W.W. Peppler, Q. Xiao, "Measurements of Capillary X-Ray Optics with Potential for Use in Mammographic Imaging", *Medical Physics*, Vol 22, Iss 11, pp 1793-1801, 1995.

¹³Lei Wang, B.K. Rath, W.M. Gibson, J.C. Kimball, C.A. MacDonald, "Performance Study of Polycapillary Optic Performance for Hard X rays," Journal of Applied Physics, **80** (7), pp.3628-3638, October 1, 1996

¹⁴F.A. Hofmann, C.A. Freinberg-Truffas, S.M. Osens, S.D. Padiyar, C.A Macdonald, "Focusing of Synchrotron Radiation with Polycapillary Optics," Beam Interactions with Materials and Atoms: Nuclear instruments and Methods B, vol. **133**, pp. 145-150. 1997.

¹⁵B.K. Rath, W.M. Gibson, Lei Wang, B.E. Homan, and C.A MacDonald, "Measurement and Analysis of Radiation Effects in Polycapillary X-Ray Optics," Journal of Applied Physics, 83, no 12, pp. 7424-7435, 1998.

¹⁶J. D. Jackson, "Classical Electrodynamics", 1962 by John Wiley & Sons, Inc. Sect. 7.9, pp 227.

¹⁷Hui Wang, Lei Wang, W. M. Gibson, C. A. MacDonald, " Simulation Study of Polycapillary X-Ray Optics," X-ray optics, Instruments and Missions Proc. SPIE. VOL 3444, July 1998, 643-651.

¹⁸The NNDC online data service, Brookheaven National Lab Nuclear Data Center. (Remote host address: bnlnd2.dne.bnl.gov)

Table I. Fiber description and simulation parameters

Fiber					Simulation			
Fiber type	Outer Diameter m	Channel size μm	Open area %	Length m	Bending R m	Waviness w mrad	Layer t μm	Roughness z nm
A	0.53	12	60	60	40	0.26	45	1.8
B30	0.51	12	60	30	30	0.15	18	1.7
B60	0.51	12	60	60	56	0.15	35	1.7
C	0.51	11	50	60	27	0.19	33	1.8
D	0.53	11	50	60	28	0.2	43	1.8
E	0.53	11	40	60	45	0.28	47	2.1

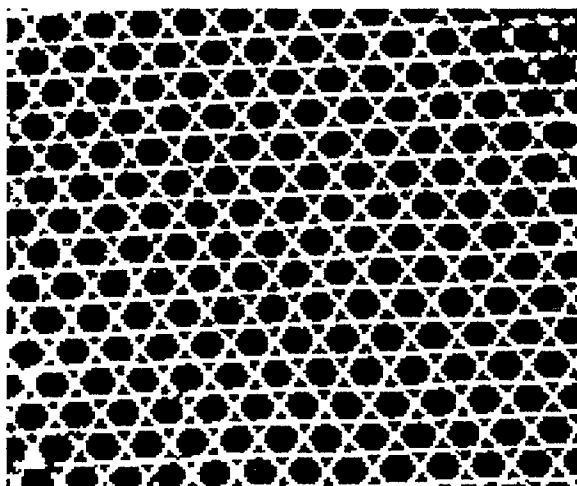


Figure 1. Photograph of a sample cross-section of leaded glass polycapillary fiber with channel diameter of $12 \mu\text{m}$ and fractional open area of 60%.

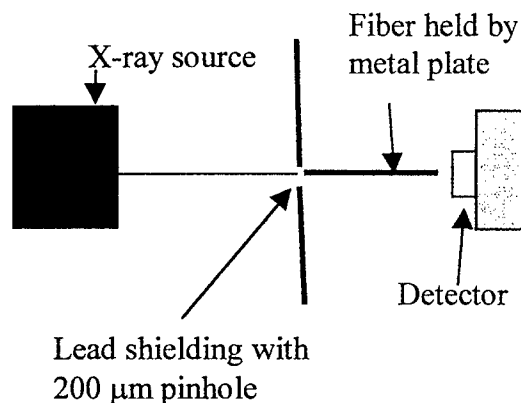


Figure 2. Experimental Setup for fiber measurement

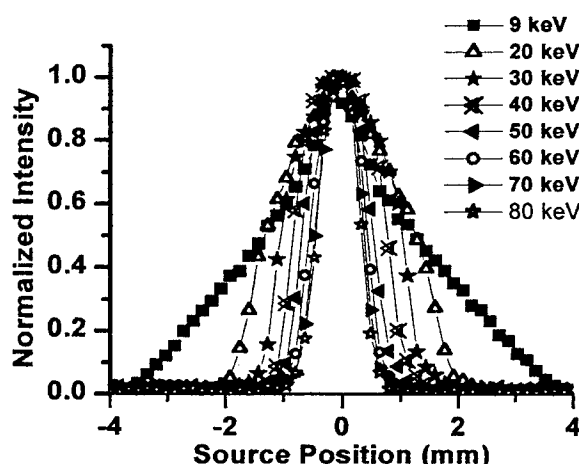


Figure 3. Normalized transmission vs source position, taken by moving the source in the horizontal direction with fiber and pinhole fixed

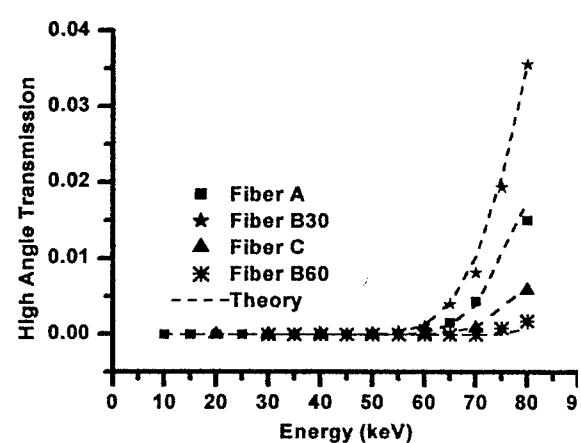


Figure 4. Large angle (cut through) transmission versus energy, measured with the source moved away from the aligned position to an angle larger than the critical angle. Dashed lines are theoretical calculations using equation 5.

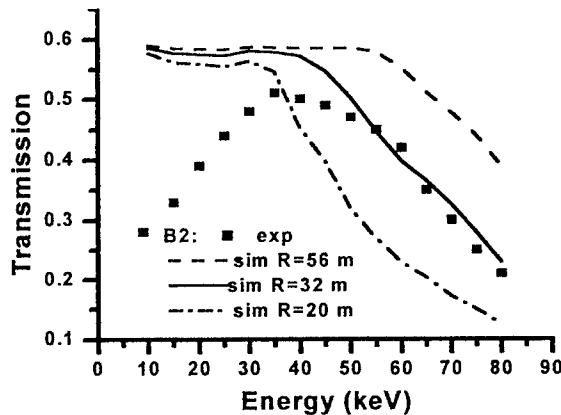


Figure 5. Simulated transmission spectra for type B60 fiber for different bending radii are compared with the experimental data. The figure shows that bending alone can not fit the data since the smallest bend underestimates the transmission at high energies.

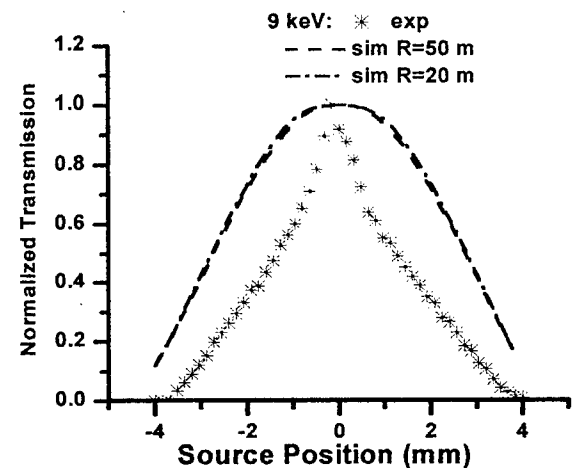


Figure 6. Simulation of source scan curves with different bending radii compared with the experimental data at 9 keV. The simulated curve does not become narrow enough even for a bend radius of $R=20$ m.

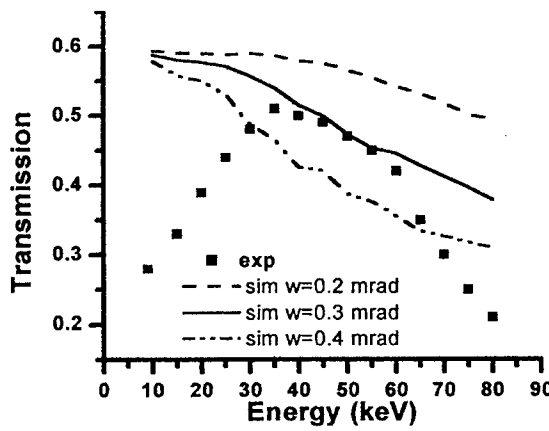


Figure 7. Simulated transmission spectra are compared with the experimental data. The waviness correction causes the transmission to drop primarily in the middle energy range.

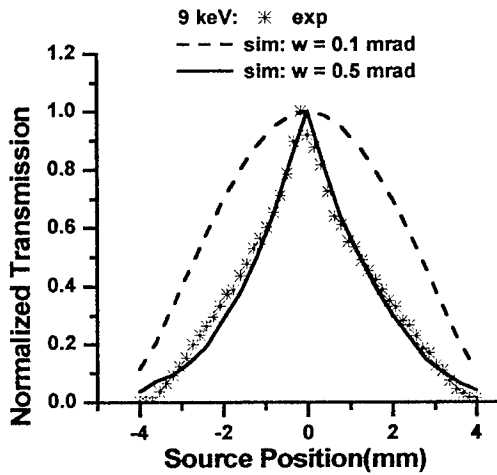


Figure 8. Simulated source scan curves with different waviness are compared with the experimental data at 9 keV. A waviness of 0.5 mrad, which is too large at higher energies, is needed to fit the data.

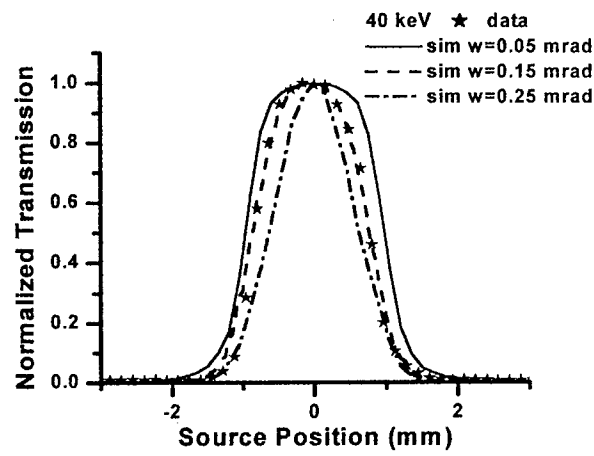


Figure 9. Simulated source scan curves with different waviness are compared with the experimental data at 40 keV. Since the simulated curve with a waviness of 0.15 mrad fits the data fairly well, it is used as the value for waviness in the best fit simulation parameters in Table I.

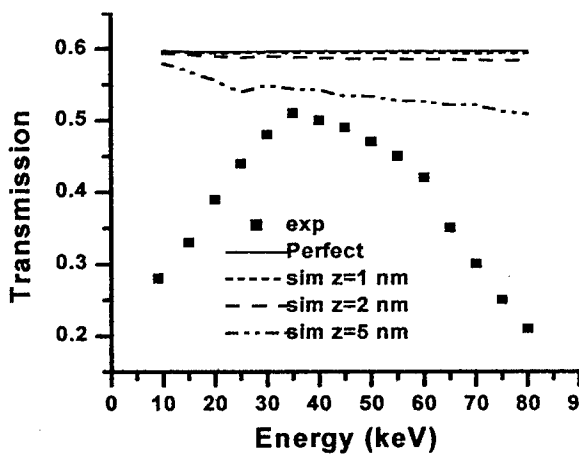


Figure 10. Simulated transmission spectra for type B60 fiber for different roughness corrections are compared with experimental data

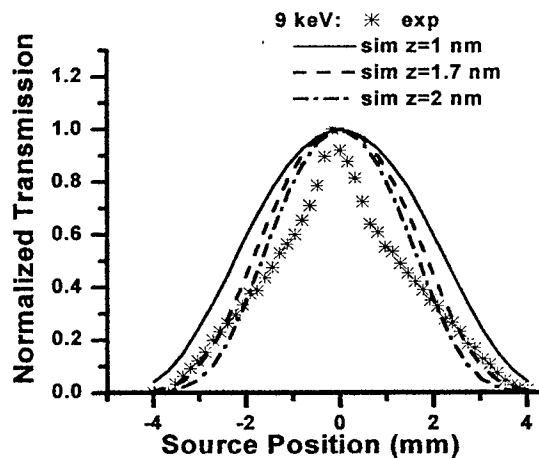


Figure 11. Simulated source scan curves for type B60 fiber for different roughness are compared with experimental data at 9 keV. The curve is too low at large displacements for the highest value of roughness.

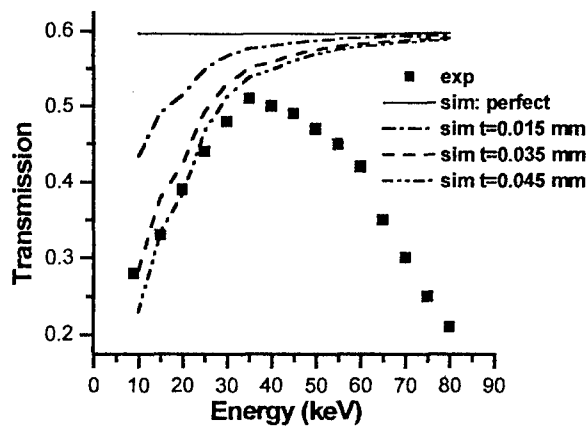


Figure 12. Simulated transmission spectra with different layer thicknesses alone compared with the experimental data. The figure shows that the maximum layer thickness for a type B60 fiber is 35 μm to fit the low energy transmission.

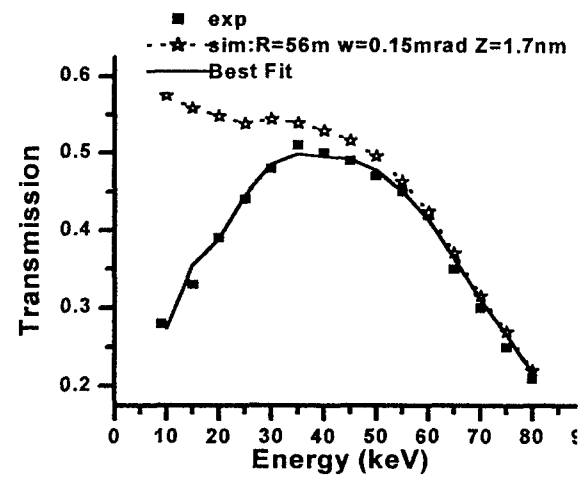


Figure 13. Simulated transmissions with and without a leaded glass filter layer for fiber B60 are compared with the experimental data. Best fit is achieved with $R=56$ m, $w=0.15$ mrad, $z=1.7$ nm, $s=6$ μm and $t=33$ μm .

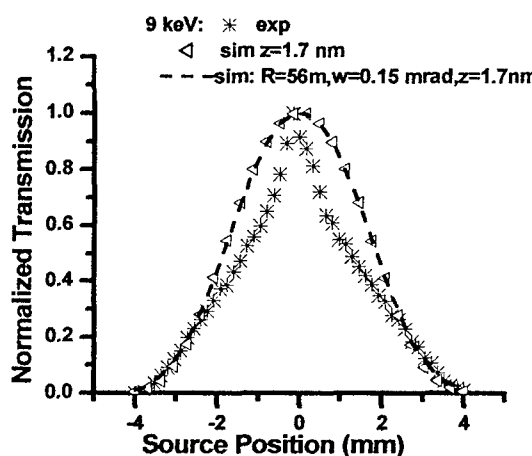


Figure 14. Simulation of source scan curves with $z=1.7$ nm, $R=56$ m, and $w=0.15$ mrad, and with roughness $z=1.7$ nm alone, compared with the experimental data. The best fit simulation does not fit the data quite well, possibly because the actual transmission at 9 keV is quite low.

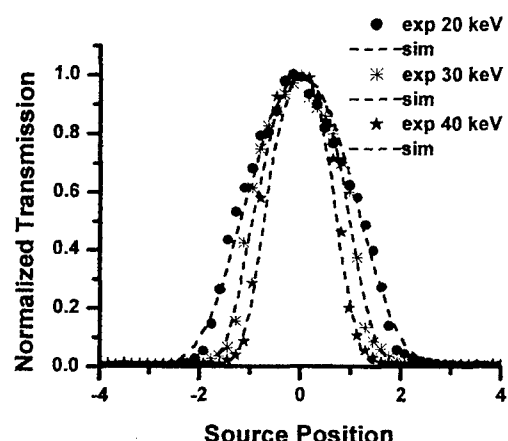


Figure 15. Simulated scan curves with best fit simulation parameters compared with the experimental data at three photon energies.

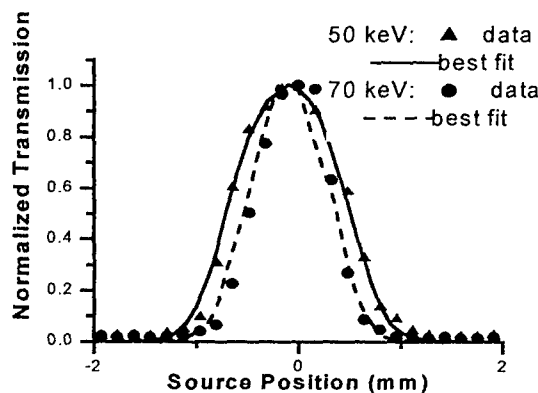


Figure 16. The simulation of scan curves with best fit parameters at 50 and 70 keVs, compared with the experimental data.

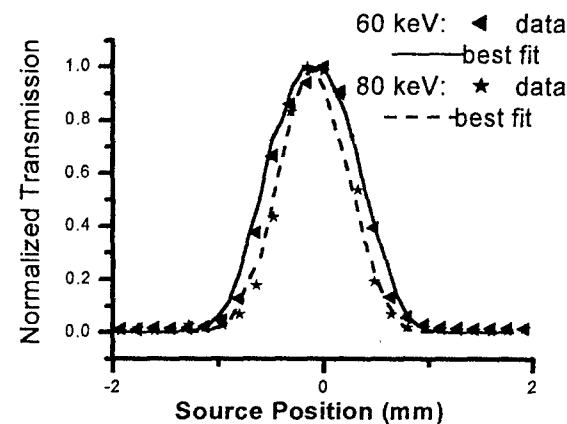


Figure 17. The simulation of scan curves with best fit parameters at 60 and 80 keVs, compared with the experimental data.

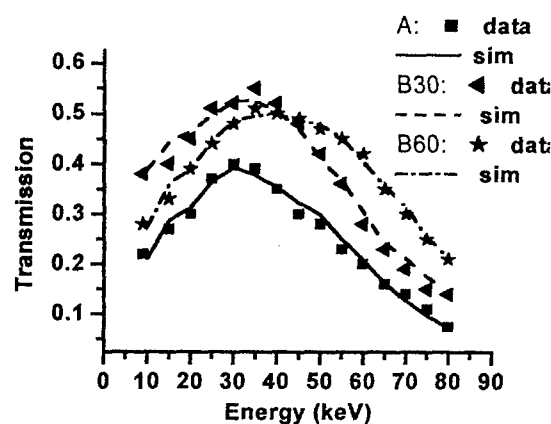


Figure 18. Simulation of transmission spectra of fiber A, fiber B60 (B with length of 60 mm) and fiber B30 (B with length of 30 mm) with their best fit parameters listed in Table I, compared with the experimental data.

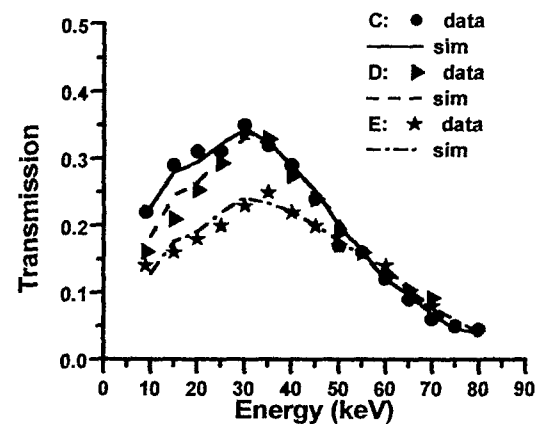


Figure 19. Simulated Transmission spectra of fiber C, fiber D and fiber E with their best fit parameters listed in Table I, compared with the experimental data.

DEVELOPMENT OF POLYCAPILLARY X-RAY OPTICS FOR SCATTER REJECTION

Suparmi, Cari, W.M. Gibson, and C.A. MacDonald
Center for X-ray Optics, University at Albany,
State University of New York,
Albany, NY 12222

1. ABSTRACT

Many medical imaging and industrial applications for x rays require large area optics with good scatter rejection. Preliminary scatter rejection and contrast measurements show that a prototype long borosilicate optic increases the contrast by a factor of 1.7 by decreasing the scatter transmission nearly a factor of 10 at 20 keV. Since borosilicate optics have higher scatter transmissions at high energies, the optics have to be fairly long to give good scatter rejection at high energies. However, long optics are complex to manufacture and have increased defect rates. Lead glass would allow the optic to be much shorter and still give good contrast enhancement, because of the superior absorption of leaded glass. In order to investigate the feasibility of using leaded glass polycapillary optics for these applications, measurements and simulations have been performed on the behavior of leaded glass polycapillary fibers in the 9-80 keV energy range. These fibers have an outer diameter of about 0.5 mm, channel diameter of 12 μm and fractional open area from 40% to 60%. The transmission efficiencies of these fibers of different types and lengths were measured as a function of source location and x-ray energy. The measurements were analyzed using a geometrical optics simulation program, which included the effects of roughness, waviness, bending and glass inclusions. Despite low transmission at low energies, leaded glass polycapillary optics with a length of 30-60 mm seem promising for many high energy (>20 keV) x-ray applications. Type B fibers with a 60 mm length have a transmission efficiency of 50% in the 35-40 keV energy range, which is 83% of fiber's open area, and very low scatter transmission of 0.18% at 80 keV. The same fiber with a shorter length of 30 mm has a transmission which is higher at lower energies, and more than 52% in the 20-40 keV energy range.

2. INTRODUCTION

Polycapillary optics, consisting of arrays of tiny hollow glass tubes with diameters on the order of few microns, is a relatively new technology for controlling x-ray beams. A polycapillary fiber is a capillary bundle with hundreds or thousands of hollow channels, as shown in figure 1. X rays striking the interior of the glass tubes at grazing incidence are guided down the tubes by total external reflection. Arrays of curved or tapered capillaries can be used to focus, collimate and filter x-ray radiation. Polycapillary optics have

potential usefulness in many applications, including x-ray lithography, medical imaging, crystallography and astronomy.¹⁻³ Properties of borosilicate polycapillary fibers, fabricated optics, and their applications have been studied extensively in the 8-80 keV energy range.⁴⁻¹¹ Borosilicate single fibers with a length of 140 mm have good transmission, but also have a large high-angle scatter transmission of 16% at energy 80 keV.¹² Scatter rejection and contrast measurements using a tapered borosilicate glass optic are presented. Since borosilicate optics have high scatter transmission at higher energies, the optics would need to be very long to provide good scatter rejection for high-energy applications. However, long optics lead to complexity in manufacturing, expense and increased defect rate. For many applications of scatter rejection optics, large areas are necessary and large area long optics are practically difficult to produce. Since shorter optics are easier to manufacture, optics with a shorter length would

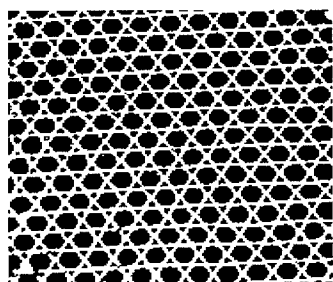


Figure 1. Photograph of a cross-section of a leaded glass polycapillary fiber with channel diameter of 12 μm and fractional open area of 60%.

- SPIE, Vol. 4144, Advances in Laboratory-Based X-Ray Sources and Optics, Conference Chairs: Carolyn A. MacDonald, Univ. At Albany, Ali Khounsary, Argone National Lab.

provide a faster route to bringing the benefit of polycapillary x-ray optics to these applications. Leaded glass optics are advantageous for excellent scatter rejection compared to borosilicate glass because of their superior absorption. To explore the potential of lead glass scatter rejection optics, the transmission for variety of leaded glass single fibers was measured in the energy range from 9 to 80 keV. The results were analyzed using a geometrical optic simulation program. The use of the simulation to analyze the experimental data for 60 mm-long type B fibers is demonstrated. The fitting process was used to determine the best-fit parameters of the simulation for five other leaded glass fibers.

3. BASIC PRINCIPLE

Capillary x-ray optics use multiple total external reflections to guide grazing incidence x rays in arrays of tiny hollow glass tubes. For the leaded glass capillaries that were used in the experiments described here, the critical angle for reflection is¹³

$$\theta_c = 35 \text{ (mrad) / } E \text{ (keV)}, \quad (1)$$

The higher the photon energy, the smaller is the critical angle.

4. CONTRAST ENHANCEMENT USING BOROSILICATE POLYCAPILLARY OPTICS

4.1 Experimental Setup

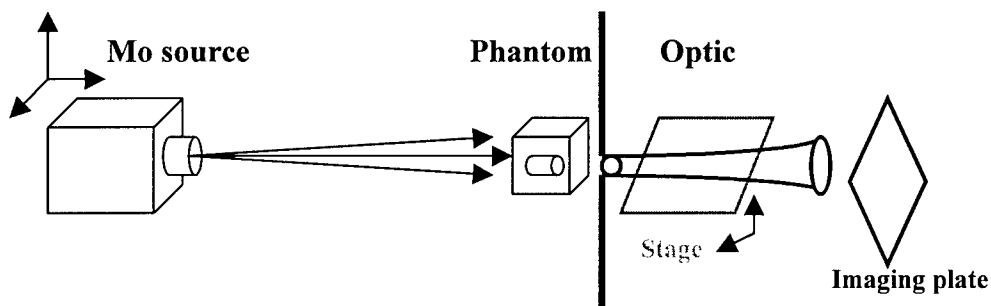


Figure 2. Experimental setup for scatter rejection and contrast measurements

The experimental setup for scatter rejection and contrast measurements is shown in figure 2. The x-ray generator used in the experiment was a Mo source with a 300 μm source spot size and maximum operating voltage of 35 kVp. The source head was mounted on two stages which could be translated in the two directions transverse to the x-ray beam. Thick lead shielding was used to prevent background x rays from reaching the imaging plate. The borosilicate monolithic optic was put on aluminum plate and covered by powder filling to prevent x-ray leakage around the optic. A Fuji imaging plate with 50 μm resolution was used to record the image. The Lucite phantom used in the contrast measurement was 45 mm thick. Several lead strips with different width were attached to the phantom to measure scatter transmission.

4.2 Optic

A prototype borosilicate monolithic optic, 166 mm in length, with input diameter of 4.5 mm and 7.6 mm output, was used to measure scatter fraction and contrast enhancement of a Lucite phantom with a thickness of 45 mm. The transmission of the whole optic was 35% at 20 keV and 7% at 60 keV. A central part of the optic, 4 mm in diameter at the output, has good transmission up to energy 40 keV.

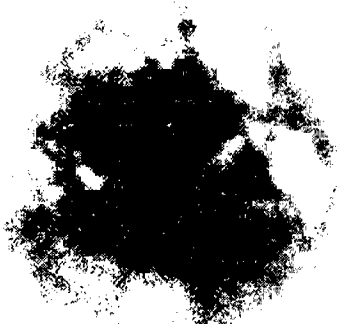


Figure 3. Output uniformity of a long monolithic optic, $L=166$ mm, $D_{\text{input}}=4.5$ mm, $D_{\text{output}}=7.6$ mm

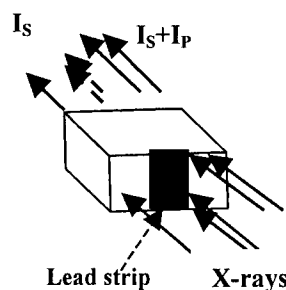


Figure 4. Sketch of x-ray paths for scatter measurement.

The output uniformity of the optic is shown in figure 3. The channels of the outer part of the optic, which does not transmit well, may be blocked by glass inclusions. Such an optic provides magnification, and thus enhanced resolution, as well as reducing scatter.

4.3 Scatter fraction Measurement

To measure the scatter transmission of the optic, several lead strips with different width but the same thickness were attached to the phantom, as shown in figure 4. The scatter fraction, S_F , was calculated using formula

$$S_F = I_S / (I_S + I_p) \quad (2)$$

where I_S is the intensity behind the lead strip (scatter intensity) and I_p is the primary intensity, which is the intensity around the lead strip subtracted by scatter intensity. The optic reduced the scatter fraction by nearly a factor of 10, as shown in figures 5a and 5b.

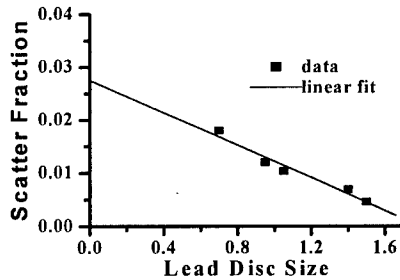


Figure 5a. Scatter fraction with optic.

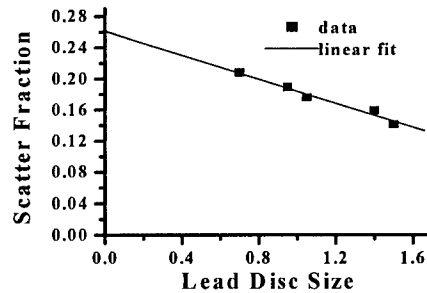


Figure 5b. Scatter fraction without optic.

4.4 Contrast Measurements

The Lucite phantom used in the contrast measurements was 45 mm thick and had four holes with the same diameter of 1.5 mm and different depths, from 10 mm to 35 mm, as listed in Table I. The diameter of the holes were smaller than the central area the optic which transmits well. Each image was taken on a single hole. A sketch of the Lucite phantom with two of the holes is shown in figure 6. The contrast was measured with and without optic. The images with and without the optic are shown in figures 7a and 7b. The contrast, C , is

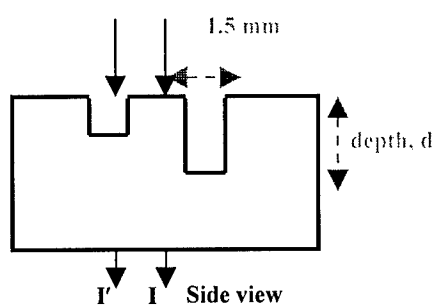


Figure 6. Sketch of Lucite phantom

$$C = \ln (I'/I) \quad (3)$$

- SPIE, Vol. 4144, Advances in Laboratory-Based X-Ray Sources and Optics, Conference Chairs: Carolyn A. MacDonald, Univ. At Albany, Ali Khounsary, Argone National Lab.

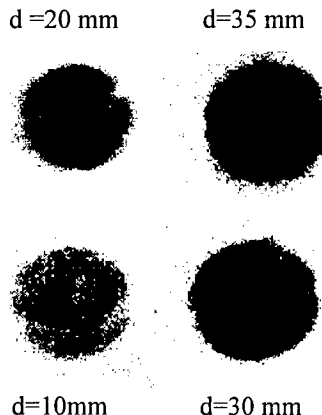


Figure 7a. Lucite phantom image with optic.

Hole depth, d (mm)	Contrast		Ratio
	With optic	No optic	
35	3.1±0.1	2.4±0.03	1.3±0.1
30	2.6±0.1	1.9±0.04	1.4±0.1
20	2.1±0.1	1.4±0.1	1.5±0.1
10	1.2±0.03	0.7±0.02	1.7±0.02

Table I. Contrast and contrast enhancement

be cheaper. In the following section, several leaded glass fibers were measured and analyzed using a geometric simulation.

5. GEOMETRIC SIMULATION

In the geometrical optic simulation used in this article, x-ray transmission through hollow glass fibers is simulated by tracing a large number of x rays through fibers. The simulation includes four fiber quality defects: roughness; waviness; channel blockage; and also profile corrections that can be approximated by uniform bending. It had been shown previously that geometric simulations with these four best parameters are in good agreement with experimental data for borosilicate single fibers at 1- 80keV.^{10, 11, 15}

The geometric algorithm is a two dimensional approximation. Because of the small critical angle, the velocity of the x-ray photon along the capillary axis is nearly equal to c , the velocity of light. The trajectory of an x ray can be reduced to the two dimensional motion inside the capillary cross section.¹⁰ Deviations of the channel from a straight path are approximated by uniform bending described by a bending radius, R . The bending of the channel makes the apparent motion of the x ray within the channel cross section similar to that of a classically accelerated particle.

Surface roughness is formally parameterized by a correlation length and root-mean square displacement of the rough surface, z . Because changes in the correlation length change the effective roughness height, and due to the lack of actual correlation data, the correlation length was fixed at $6 \mu\text{m}$ for all simulations. Changing this value would cause a proportional scaling all of reported roughness heights. The value was chosen for borosilicate fibers so that the roughness heights agree with atomic force microscopy data.¹⁰ The surface roughness decreases the apparent reflectivity of the channel walls and therefore the transmission in capillary channels. The third capillary surface quality parameter is waviness, which occurs on a spatial range

where I is the intensity near the hole and I' is the intensity through the hole. The contrast with and without the optic, and also contrast enhancement, are listed in Table I. The contrast enhancement is the ratio of the contrast with and without the optic. The results show that the

optic increases the contrast by a factor of 1.7 for the shallowest hole. The images in figures 7a and b are shown to scale. A magnification of 1.8 was obtained with the optic. This long monolithic optic with small area was used to magnify the image, reduce the scatter transmission and enhance the contrast.

4.5 Disadvantages of Long Borosilicate Optics

Long optics, even with small input area, tend to have defects as shown in figure 3. A long optic also leads to manufacturing complexity and expense. Improvements in the technology of fabricating monolithic optics have been achieved.¹⁴ Medical imaging or astronomy applications, however, require large area optics. For high-energy applications, borosilicate optics need to be quite long. Leaded glass would allow the optic to be much shorter and still good give scatter rejection because of strong absorption of lead glass. The shorter optics are easier to manufacture and could

shorter than the capillary length and longer than roughness. The average effect of the waviness can be considered as a random tilt of glass wall. In the simulation, these tilt angles are normally distributed with a mean value of zero and a standard deviation w . The fourth polycapillary defect is channel wall blockage, which is modeled by a filter layer of glass of thickness t .

6. MEASUREMENTS OF LEADED GLASS FIBERS

6.1 Experimental Apparatus

The experimental apparatus is shown in figure 8.

6.1.1. Source

The x-ray generator used in the experiment was a low current Microfocus MS50 with a 50 μm spot size, tungsten target, and a maximum operating voltage of 100 kVp. The source head was mounted on a stage which could be moved in the two directions transverse to the x-ray beam.

In order to reduce the background of x rays, this movable source was enclosed in a 6-mm-thick lead

box with a 100x175 mm aperture in the front. The source to fiber distance was 1100 mm. In the measurement for photons with energy higher than 50 keV, a 5-mm-thick aluminum plate was used as a filter between the source and the fiber to remove the low energy photons, and reduce the dead time in the detector.

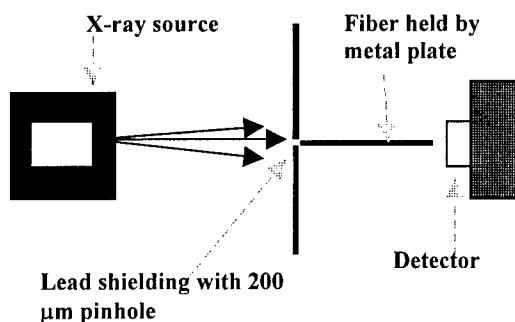


Figure 8. Experimental setup for fiber measurement.

The pinhole was smaller than the fiber but still covers hundreds or more channels. Its small size was chosen not only to avoid the leakage around the fiber and reduce dead time in the detector, but also to keep the source-fiber distance as small as possible while keeping the photon entrance angle at the edges of the pinhole to less than the critical angle at energies up to 80 keV.

6.1.3. Fiber

The fiber was held straight by a finely machined groove in an aluminum plate and covered by iron powder to prevent x-ray leakage around the fiber. The aluminum plate was also mounted on a stage which can be translated in two orthogonal directions transverse to the beam. All stages were mounted on rail carriers, which could be moved along the beam directions. Five kinds of fibers, listed in Table II, were measured. The outer cross sections of all the fibers are roughly hexagonal.

6.1.4. Detector

The detector was a high purity germanium detector with about 200 eV resolution at 5.9 keV and 550 eV at 122 keV. The detector was placed behind the fiber. The distance between the source and detector was fixed to keep air absorption constant. Motion control and data collection were all controlled with a small computer.

7. RESULTS AND ANALYSIS FOR LEADED GLASS FIBERS

7.1. High-angle Transmission

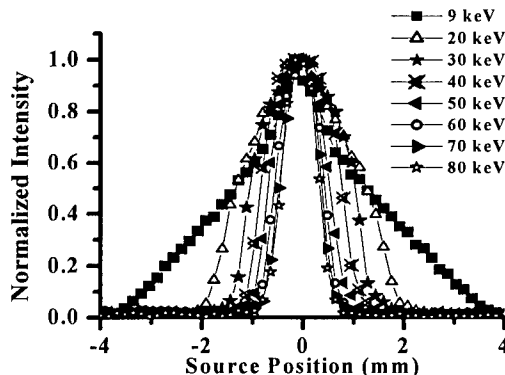


Figure 9. Normalized intensity vs source position, taken by moving the source in the horizontal direction perpendicular to the fiber with fiber and pinhole fixed.

The pinhole was located in the center of the fiber to avoid leakage. Figure 9 shows a source scan plot of transmission as a function of source location for eight different energy windows of approximately 2 keV in width. The transmission plots are narrower for the higher energy windows, as expected due to the decrease in critical angle with photon energy. For leaded glass fibers, because of the high absorption of lead, the background signal from photons with incidence angle greater than the critical angle is very small. Most of these photons are absorbed rather than cutting through the glass wall. The cut through transmission is 3.6% at 80 keV for a 30-mm-long type B fiber and 0.18 % for a 60-mm-long fiber. Measured and theoretical high-angle transmission at several energies are shown in figure 10. The theoretical values are calculated as

$$T_c = \exp \{ -L (1-f) \mu \rho \} \quad (4)$$

where L is the fiber length, f is the fractional open area of the fiber, ρ is the density of the glass, and μ is the mass absorption coefficient of the glass obtained from the tabulated values.¹⁶ The transmission results which follow are channel transmissions from which the very small high angle cut through and fluorescence background have been subtracted.

7.2. Simulation Analysis

Table I. Fiber description and simulation parameters

Fiber type	Fiber					Simulation			
	Outer Diameter mm	Channel size μm	Open area %	Length mm	Bending R m	Waviness w mrad	Layer t μm	Roughness z nm	
A	0.53	12	60	60	40	0.26	45	1.8	
B30	0.51	12	60	30	30	0.15	18	1.7	
B60	0.51	12	60	60	56	0.15	33	1.7	
C	0.51	11	50	60	27	0.19	33	1.8	
D	0.53	11	50	60	28	0.20	43	1.8	
E	0.53	11	40	60	45	0.28	47	2.1	

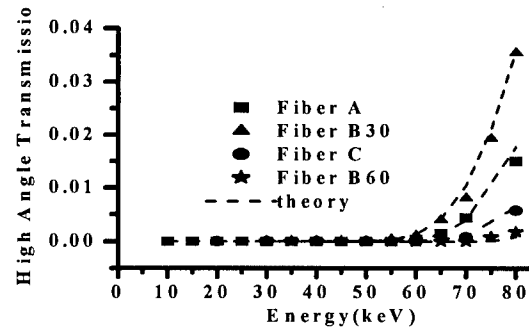


Figure 10. Large angle (cut through) transmission versus energy, measured with the source moved away from the aligned position to an angle larger than the critical angle. Dash lines are theoretical calculation using equation 4.

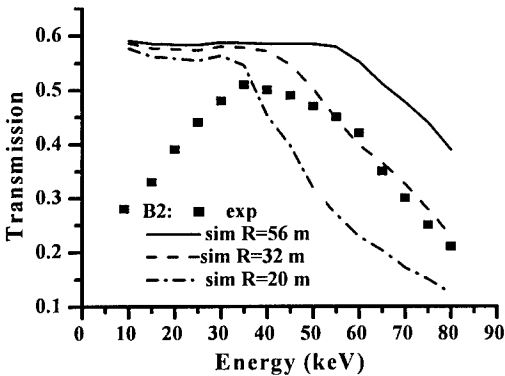


Figure 11. Simulated transmission spectra of a type B60 fiber for different bending radii are compared with the experimental data. The figure shows that bending alone can not fit the data since the smallest bend underestimates the transmission at high energies.

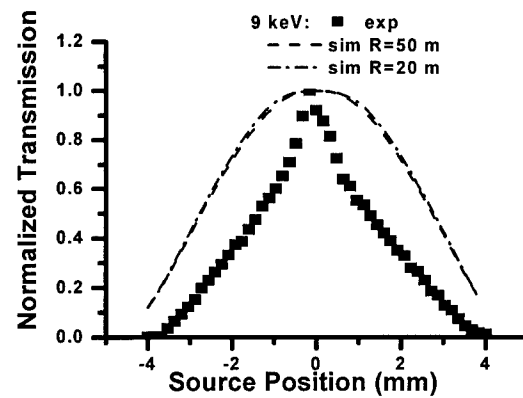


Figure 12. Simulation of source scan curves with different bending compared with the experimental data at 9 keV. The simulated curve does not become narrow enough even for a bend radius of R=20 m.

Transmission for the leaded glass fibers in Table II was measured in the energy range 9- 80keV. To illustrate the effect of each simulation parameter, the application of the simulation to the experimental data for fiber type B60 (a 60 mm-long type B fiber) is discussed in this section.

7.2.1. Bending effects

A slight bending can dramatically reduce the transmission at the high energies because of the small critical angles. The measured transmission as a function of energy along with the simulation of different radii for a type B60 fiber is shown in figure 11. The simulation with bending alone can not fit the experimental data since at smallest radius the transmission is too high at lower energies and too low at high energies. Since any waviness correction will reduce the transmission, the radius of bend has to be larger than 32 m. Simulations with different bending radii and the experimental transmission source scan at 9 keV are shown in figure 12. Even with a sharp bend, the simulated transmission source scan at 9 keV is not narrow enough.

7.2.2. Waviness effect

Simulations with different waviness corrections are compared to the experimental data of transmission spectra in figure 13. The waviness alone can not fit the data. The simulation shows that the waviness causes

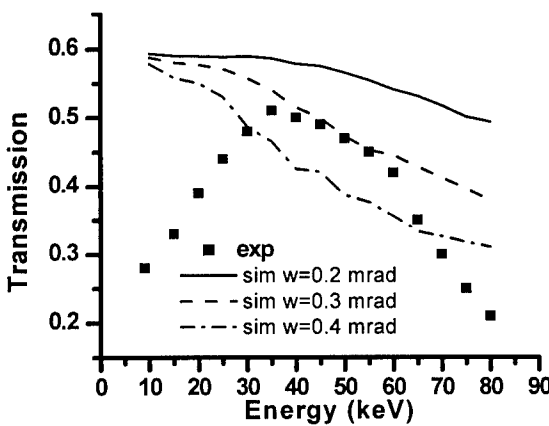


Figure 13. Simulated transmission spectra are compared with the experimental data. The waviness correction causes the transmission to drop primarily in the middle energy range.

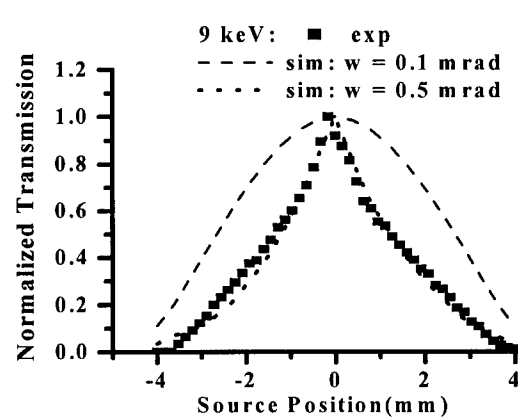


Figure 14. Simulated source scan curves with different waviness are compared with the experimental data at 9 keV. A waviness of 0.5 mrad, which is too large at higher energies, is needed to fit the data.

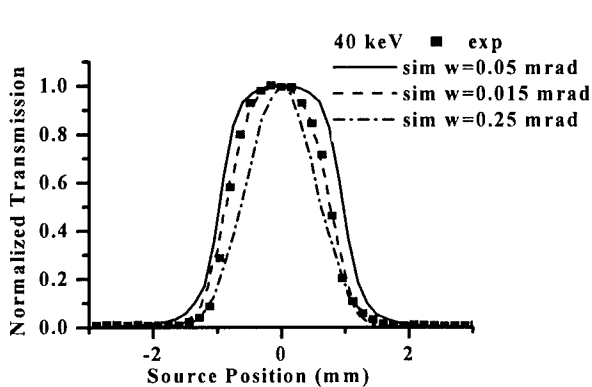


Figure 15. Simulated source scan curves with different waviness are compared with the experimental data at 40 keV. Since the simulated curve with a waviness of 0.15 mrad fits the data fairly well, it is used as the value for waviness in the best fit simulation parameters in Table I.

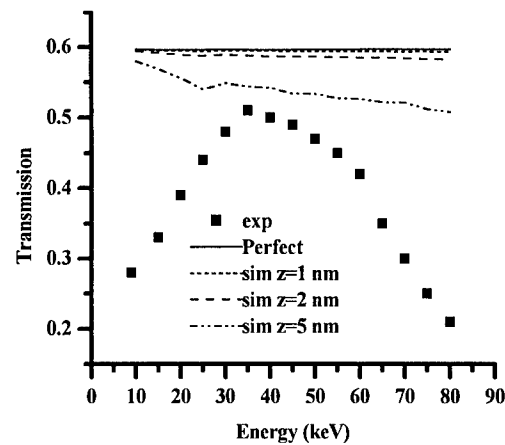


Figure 16. Simulated transmission spectra for a type B60 fiber for different roughness corrections are compared with experimental data.

the transmission to drop rapidly at medium energies but not rapidly enough at higher energies. Figure 13 shows that the waviness correction has to be smaller than 0.3 mrad to fit the data. Simulated transmission source scans with different waviness are compared to the experimental data at 9 keV in figure 14. The simulation with a waviness of 0.5 mrad fits the spectrum source scan fairly well at 9 keV. However, that was seen to be too large for the transmission spectrum of figure 13. Figure 15 compares the experimental data to simulations at 40 keV, and shows that the maximum value of waviness is 0.15 mrad.

7.2.3 Roughness effects

Simulations of the transmission of fiber type B60 with and without roughness corrections are compared to the experimental data in figure 16. For a perfect capillary, the transmission spectrum is flat, since the distance between the source and the fiber is large enough to ensure that every photon which hits the glass wall has grazing angle smaller than its critical angle. The transmission is almost flat at all energies, but for high roughness drops more rapidly at medium energies than at high energies. The transmission drop depends on both the surface reflectivity, which is reduced by roughness, and the number of reflections that the photon undergoes through the channel. The transmission is proportional to R^n where R is reflectivity, and n is the number of bounces. For a straight capillary, the average number of bounces of the photon along the channel is small, usually less than three. Thus the roughness has only a fairly small effect on the transmission spectrum in figure 16. The transmission as a function of source location at 9 keV is shown in figure 17. Because photons experience more than 21 reflections for large source displacements, the

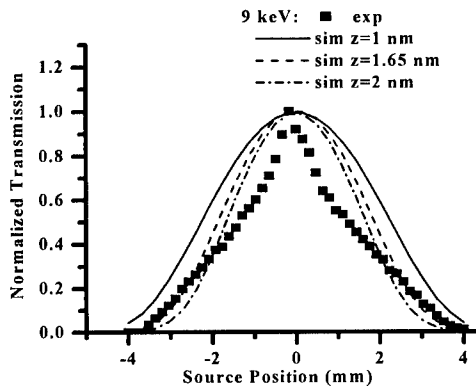


Figure 17. Simulated source scan curves for a type B60 fiber for different roughness are compared with experimental data at 9 keV. The curve is too low at large displacements for the highest value of roughness.

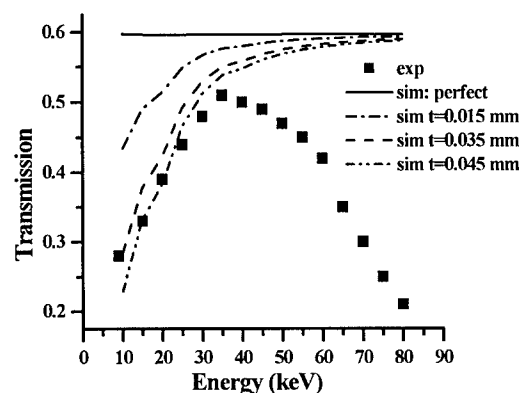


Figure 18. Simulated transmission with different layer thicknesses alone compared with experimental data. The figure shows that the maximum layer thickness for a type B60 fiber is 35 μm to fit the low energy transmission.

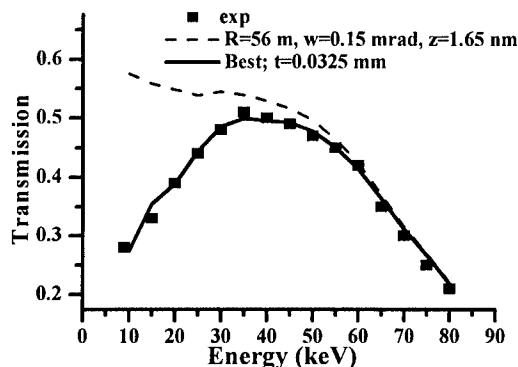


Figure 19. Simulated transmissions with and without leaded glass filter for type B60 fiber are compared with the experimental data. Best fit is simulated transmission with $R=56$ m, $w=0.15$ mrad, $z=1.7$ nm, and $t=33$ μ m.

transmission at high angles is sensitive to roughness. The transmission is too small if the roughness is larger than 1.7 nm.

7.2.4. Channel blockage

By modeling channel blockage with a glass filter layer of thickness $t=35$ μ m, the simulated transmission spectrum with the glass layer alone fits the data at low energies. The simulated transmission spectra with different layer thicknesses are compared with the experimental data in figure 18.

To fit the high energy transmission spectrum data, finally, we combine the waviness determined from source scan at 40 keV, the roughness from source scan at 9 keV, and add the bending radius, that must be larger than 32 m, to achieve the simulation shown in figure 19. To fit the experimental data for whole spectrum, the simulation must also include absorption by a leaded glass layer, which models glass debris in the channels. As shown in figure 19, the inclusion of a 33 μ m thick leaded glass layer gives a good fit with the experimental transmission spectrum.

The best fit simulation compared to the experimental source scan curves are shown in figures 20-23. The simulated transmission source scan curves fit the data fairly well at energies from 20 to 80 keV. The source scan at 9 keV does not fit the simulated transmission, as shown in figure 20. This may be partly because the actual value of the transmission at 9 keV, as shown in figure 19, is quite low.

7.2.5 Simulation summary

The primary effect of bending is to reduce the transmission at high energies. Channel blockage reduces the transmission at low energies. Roughness reduces the width of source scan at low energies. Waviness

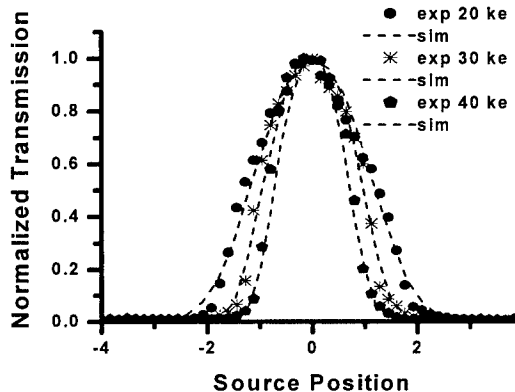


Figure 21. Simulated scan curves compared with the experimental data at three photon energies.

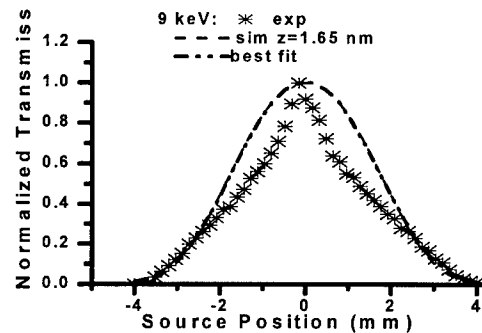


Figure 20. Simulation of source scan curves with $z=1.7$ nm, $R=56$ m, and $w=0.15$ mrad, and with roughness $z=1.7$ nm alone, compared with the experimental data. Since the actual transmission at this energy is quite low, the source scan curve might be somewhat distorted, and thus the simulation does not fit the data well.

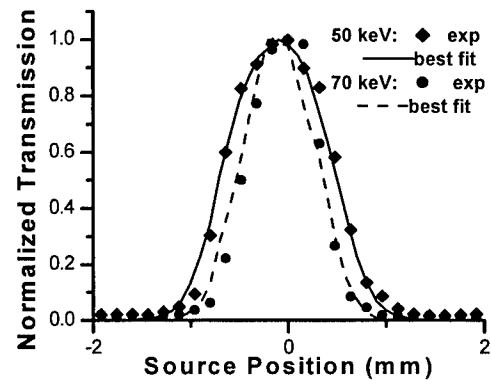


Figure 22. The simulation of scan curves with best fit parameters at 50 and 70 keV, compared with the experimental data.

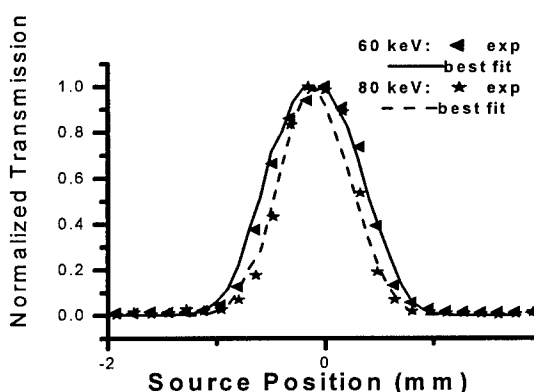


Figure 23. The simulation of scan curves with best fit parameters at 60 and 80 keV, compared with the experimental data.

Fiber type B has high open area, low channel blockage, and the least bending and waviness. Thus this fiber has better transmission than other fibers. Figure 24 shows that the transmission of this fiber type with a shorter length (B30) is higher at lower energies because of its thinner blockage layer. This is consistent with a statistically random model of glass inclusion. Because of its high flexibility, the shorter fiber experiences more bending than the longer fiber, and thus the transmission falls off faster at higher energies. The shorter fiber has a higher scatter cut through, as shown in figure 10. The different open area, bending, waviness and blocked channels cause the differences in the transmission among the fibers. Fiber type C and D have the same open area, but fiber type C has thinner glass layer, as listed in Table II. As a result, fiber type C has higher transmission at lower energies than fiber type D, as shown in figure 25.

primarily reduces the transmission and the source scan width at mid range energies.

7.3. Fiber Results

Using the fitting processes described above, the best fit simulation parameters for fibers A, C, B60, D and E, which have length 60 mm, and also fiber B30, which has length 30 mm, were obtained. The best fit simulation parameters are listed in Table II. The best fit simulated transmissions along with the experimental data are shown in figures 24 and 25. The outer diameter of the fibers are in the 0.51- 0.53 mm range. These fibers are thin and flexible, and therefore are difficult to keep straight in the measurement apparatus, resulting in sharp bending radii and relatively poor high-energy transmission.

8. CONCLUSIONS

The borosilicate optic increased the contrast in a Lucite phantom image by a factor 1.7 by removing the scatter. However, to provide good scatter rejection at high energies, borosilicate optics have to be fairly long which leads to an increased defect rate. The strong absorption of leaded glass allows the optics to be much shorter. Measurements were performed on leaded glass fibers to asses the potential for leaded glass

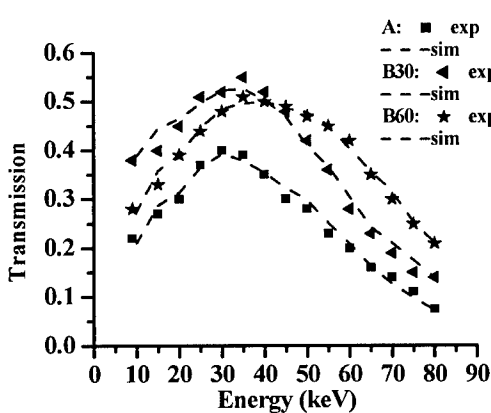


Figure 24. Simulation of transmission spectra of fiber A, fiber B60 (B with length of 60 mm) and fiber B30 (B with length of 30 mm) with their best fit parameters listed in Table II, compared with the experimental data.

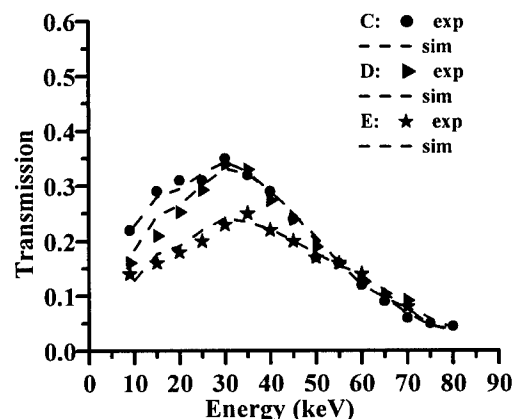


Figure 25. Simulated Transmission spectra of fiber C, fiber D and fiber E with their best parameters listed in Table II, compared with the experimental data.

scatter rejection optics. The high measured transmission (>45%) for fiber type B shows that the performance of this leaded glass fiber is quite good in the 25-50 keV energy range. The geometric simulation, with roughness, waviness, bending and channel blockage corrections, performs well in explaining the measured transmission spectra above 15 keV. According to this simulation, bending is the most harmful at higher energies, and glass inclusions that block the channels are harmful at lower energies. For type B fibers, even though the roughness is high, the waviness is low and the bending radius is the largest among the fibers. The high-energy transmission performances could be improved by making the fiber diameter larger and therefore more rigid to minimize unintentional bending. Low energy performance is improved by using shorter fibers. Because of the good absorption of lead, the high-energy photons, which are not reflected, are absorbed completely by 60 mm-long fibers, even at 80 keV. The high-angle transmission at 80 keV is only 0.2%. This high-angle transmission is very much less than the 16% for a longer (140 mm) borosilicate fiber. Thus short leaded glass polycapillary x-ray optics are very promising for scatter rejection in high-energy applications.

9. ACKNOWLEDGEMENT

The authors wish to acknowledge assistance from Lei Wang, Hui Wang, Michael Gubarev, Frank Hoffman, Christine Russell, C.A. Freinberg-Trufas, Francisca Sugiro and Sushil Padiyar. The Department of Army Breast Cancer Research Project grant DAMD17-97-1-7304, and NIH grants supported this work.

10. REFERENCES

- ¹ W. M. Gibson, C. A. MacDonald and M. A. Kumakhov, "The Kumakhov Lens: A New X-ray and Neutron Optics with Potential for Medical Applications", in **Technology Requirements for Biomedical Imaging**, (S. K. Mun, R. von Hanwehr and P. Gerity, ed.), IEEE Proc. 2580, 164-169 (1991).
- ² W. M. Gibson and M. A. Kumakhov, "Application of X-ray and Neutron Capillary Optics", in **X-ray Detector Physics and Applications**, (R. B. Hoover, ed.), SPIE Proc., 1736, (1992).
- ³ W. M. Gibson, and M. A. Kmakhov, "X-ray Optics", in **Yearbook of Science and Technology**, (McGraw Hill, New York), pp. 488-490, (1993).
- ⁴ W.M. Gibson and C.A. MacDonald, "Polycapillary Kumakhov Optics: A Status Report", **X-Ray and UV Detectors**, SPIE vol. 2278, pp. 156-167, (1994).
- ⁵ C.A. MacDonald, C.C. Abreu, S. Budkov, H. Chen, X. Fu, W.M. Gibson, Kardiawarman, A. Karnaughov, V. Kovantsev, I. Ponomarev, B.K. Rath, J.B. Ullrich, M. Vartanian, Q. F. Xiao, "Quantitative Measurements of the Performance of Capillary X-Ray Optics", **Multilayer and Grazing Incidence X-Ray/EUV Optics II**, (R.B. Hoover and A. Walker, ed.), SPIE Proc. vol. 2011, pp. 275-286, (1993).
- ⁶ J.B Ullrich, V. Kovantsev, C.A. MacDonald, "Measurements of Polycapillary X-Ray Optics", *Jour. Appl. Phys.*, **74** (10), Nov. 15, pp. 5933-5939, (1993)
- ⁷ C.C. Abreu, D.G. Kruger, C.A. MacDonald, C.A. Mistretta, W.W. Peppler, Q. Xiao, "Measurements of Capillary X-Ray Optics with Potential for Use in Mammographic Imaging", *Medical Physics*, Vol 22, Iss 11, pp 1793-1801, (1995).
- ⁸ Kardiawarman, B.R. York, C. Qian, Q.F. Xiao, W.M. Gibson, and C.A. MacDonald, "Application of a Multifiber Collimating Lens to Thin Film Structure Analysis", **X-Ray and Ultraviolet Sensors and Applications**, SPIE vol. 2519, pp. 197-206, (1995).
- ⁹ Lei Wang, C.A. MacDonald, "Measurement of Capillary Optic Performance for Hard X rays", **X-Ray and Ultraviolet Sensors and Applications**, SPIE vol. 2519, pp. 219-223, (1995).
- ¹⁰ Lei Wang, B.K. Rath, W.M. Gibson, J.C. Kimball, C.A. MacDonald, "Performance Study of Polycapillary Optic Performance for Hard X rays," *Journal of Applied Physics*, **80** (7), pp.3628-3638, October 1, (1996).
- ¹¹ Lei Wang, C. A. MacDonald, and W. W. Peppler, "Performance of Polycapillary Optics for Hard X-ray Imaging," accepted, *Medical Physics*.

SPIE, Vol. 4144, Advances in Laboratory-Based X-Ray Sources and Optics,
Conference Chairs: Carolyn A. MacDonald, Univ. At Albany, Ali Khounsary, Argone National Lab.

¹² Cari, Suparmi, S.D. Padiyar, W.M.Gibson, C.A. MacDonald, C.D. Alexander, M.K. Joy, C.H. Russel, and Ze Wu Chen, "Characterazation of a Long Focal Length Collimating Lens For Hard X-Rays" in this SPIE volume.

¹³ J. D. Jackson, "Classical Electrodynamics", by John Wiley & Sons, Inc. Sect. 7.9, pp 227, (1962).

¹⁴ F.R. Sugiro, S.D. Padiyar and C. A. MacDonald, "Characterazation of Pre- and Post-Patient X-Ray Polycapillary Optics for Mammographic Imaging," in this SPIE volume.

¹⁵ Hui Wang, Lei Wang, W. M. Gibson, C. A. MacDonald, " Simulation Study of Polycapillary X-Ray Optis," X-ray optics, Instruments and Missions Proc. SPIE. Vol. 3444, 643-651, (1998).

¹⁶ The NNDC online data service, Brookheaven National Lab Nuclear Data Center. (Remote host address: bnlnd2.dne.bnl.gov.)